


Linköping Studies in Science and Technology
Dissertations No. 2217



**High-performance
Nickel-based
Superalloys
for
Additive
Manufacturing**

Jinghao Xu

Linköping Studies in Science and Technology
Dissertations No. 2217

High-performance Nickel-based Superalloys for Additive Manufacturing

Jinghao Xu (徐晴昊)



Division of Engineering Materials
Department of Management and Engineering (IEI)
Linköping University, SE-581 83 Linköping, Sweden

Linköping 2022

Opponent:

Dr. Chinnapat Panwisawas

FIMMM, FInstP, FIMechE

Associate Professor in Digital Manufacturing

Associate Director of NISCO UK Research Centre

EPSRC UKRI Innovation Fellow

NISCO UK Research Centre, School of Engineering, University of Leicester, UK

Committee members:

Dr. Yu Cao

Associate Professor at Industrial and Materials Science, Chalmers University of Technology, Gothenburg, Sweden

Dr. Greta Lindwall

Associate Professor at Department of Materials Science and Engineering, KTH Royal Institute of Technology, Stockholm, Sweden

Prof. Urban Wiklund

Professor at Department of Materials Science and Engineering, Uppsala University, Uppsala, Sweden

Date:

May 6, 2022

Location:

ACAS, Linköping University



This work is licensed under a Creative Commons Attribution 4.0 International License.

<https://creativecommons.org/licenses/by/4.0>

© Jinghao Xu

ISBN 978-91-7929-257-7 (print)

ISBN 978-91-7929-258-4 (PDF)

<https://doi.org/10.3384/9789179292584>

ISSN 0345-7524

Printed by LiU-Tryck 2022

Abstract

Additive manufacturing (AM), e.g., laser powder bed fusion (LPBF) technique, has become a powerful manufacturing process for producing metallic components with the advantages of design freedom, net-shape-forming flexibility, product customization, and reduced lead time to market. Nickel-based superalloys is one of the most significant alloy families used at elevated temperatures. Nickel-based superalloys commonly contain up to 10 more alloying elements like chromium, aluminum, cobalt, tungsten, molybdenum, titanium, and so on. The great capacity of the nickel-based superalloys for high-temperature operation is ensured by the well-tailored microstructures with the assistance of carefully doped alloying elements, and the intently developed corresponding manufacturing processes. However, high-performance nickel-based superalloys generally suffer from structural integrity issues during AM process, i.e., this class of superalloys is highly susceptible to crack. Therefore, new nickel-based superalloys adapted to AM process with tailored chemical composition are under the urgent call. Meanwhile, high-temperature performance is another prioritized target for the new superalloys.

The first topic is the chemical composition-dependent cracking mechanisms. The interdendritic region formed at the last-stage solidification has been found as the cracked spaces. Owing to the suppression of precipitate formation, the cracking mechanism is generalized as (1) the large mismatch of the solidification steps accounting for the crack initiation, and (2) the large mismatch of load-bearing capacity accounting for the crack propagation, between the dendritic and interdendritic regions. To quantitatively formulate the additive manufacturability of nickel-based superalloys, herein a two-parameter-based, heat resistance, and deformation resistance (HR-DR) model, has been successfully proposed to predict the printability on accounting for the relation between chemical composition (both major and minor elements) and cracking susceptibility. The concept of this model is formulated as that if the interdendritic region obtains both higher heat and deformation resistances than the rest dendritic region, this alloy is expected to be crack resistant. Validated by the experimental results and hitherto reported literature data, the HR-DR model provides an excellent sound prediction on the crack susceptibility of nickel-based superalloy during AM process. By considering the combination of additive manufacturability and high-temperature performance, a novel high-strength nickel-based superalloy, MAD542 has been developed based on the materials selection procedure from 921,600 candidate compositions. In addition, another precipitation-strengthened nickel-based superalloy, Alloy738+ has been developed based on the modification of the composition of heritage superalloy IN738LC, aiming for improving the additive manufacturability, creep, and oxidation resistance.

The second topic is the post-processing treatments related to microstructural evolution and mechanical properties. Owing to the thermal history during the LPBF process, the as-built microstructure commonly consists of columnar grains nearly parallel to the building

direction with strong crystallographic texture. Subjected to the post-processing treatments, the solution treatment is the key to controlling the grain evolution. It has been shown for both LPBF MAD542 and heritage LPBF CM247 superalloys, the high crystallographic texture is maintained at the sub- γ' -solvus temperatures because of the grain boundary pinning effect from grain boundary precipitates. Whilst the crystal anisotropy is highly reduced by the treatment at super- γ' -solvus temperatures driven by the means of recrystallization. However, fully recrystallized microstructure with low texture largely reduced the mechanical properties by the embrittlement manner at elevated temperatures accordingly.

The third topic is the examination of creep and oxidation performance of various LPBF superalloys. A strong building direction-dependent creep performance is found for an LPBF IN738LC superalloy fabricated by the vertical and horizontal build. Vertically built samples show 7-40 times longer rupture life and approximately 2 times longer elongation at fracture than the horizontally produced samples, for the creep at 150-300 MPa at 850 °C. To evaluate the short-term creep performance, constant displacement rate-controlled slow strain rate tensile (SSRT) testing was carried out. The constant load-controlled creep and SSRT are correlated by deformation rate-based power-law type analysis. The new superalloy LPBF MAD542 generally displays a 5 times slower deformation rate than the LPBF IN738LC superalloy at 850 °C. The new superalloy Alloy738+ shows a comparable creep performance to LPBF IN738LC. Oxidation tests were conducted at 850/950/1050 °C. The new superalloy Alloy738+ presents an excellent oxidation resistance at 850 and 950 °C. By comparison, for example, Alloy738+ has 3 times slower oxidation kinetics than IN738LC at 950 °C.

The several investigations associated with the composition/processing/property in multiple precipitation-strengthened nickel-based superalloys fabricated by AM in this thesis have proven that the materials development requires comprehensive in-depth considerations. The presented results can contribute to the fundamental understanding and/or serve as the reference data for other superalloys by AM from the properties perspective.

Keywords: Nickel-based superalloy; Alloy design; Laser powder bed fusion; Cracking susceptibility; Additive manufacturability; Heat treatment; γ' precipitate; High-temperature mechanical property; Creep; Oxidation.

Populärvetenskaplig Sammanfattning

För ungefär 13,8 miljarder år sedan, precis efter Big Bang, producerades de lättaste grundämnena: väte, helium och en liten mängd litium. Grundämnen med större massa upp till järn smiddes senare genom kärnfusion i stjärnornas hjärtan och i supernovor. De tyngre grundämnena än järn som kobolt och nickel och så vidare föddes av neutronstjärnornas sammanslagning. Blandningen av olika element skapar alla möjligheter på denna planet.

Nickelbaserad superlegering är en stor reservoar av blandningen av typer av element. Denna legering används ofta som det kritiska komponentmaterialet i högtemperaturmiljöer. Flera fördelar med valet av nickel som huvudelement kan hittas. Nickel har till exempel en relativt hög smälttemperatur (1455 °C) vilket säkerställer den inneboende högtemperaturkapaciteten, jämfört med till exempel magnesium (650 °C) och aluminium (660 °C). Nickel har ingen fastfasomvandling vid driftstemperaturerna, jämfört med till exempel titan (HCP till BCC) och järn (BCC till FCC till BCC). Nickel har en FCC-kristallstruktur som i allmänhet är mer seg än andra typer av kristaller. Nickel är ett bra lösningsmedel för att legera grundämnena. Kombinationen av element i denna legering har också stor betydelse. Till exempel hjälper tillsatsen av element som aluminium och titan bildandet av de intermetalliska föreningarna för förbättrad hållfasthet vid hög temperatur. Tillägget av matarelement som Tungsten och Molybden förbättrar motståndet mot deformation vid hög temperatur. Tillsatsen av lågmassaelement som kol och bor stärker korngränserna för dessa material.

Den senaste snabbt utvecklande additiv tillverkning (AM), även känd som tredimensionell (3D) utskrift erbjuder en unik tillverkningsprocess för att producera metallkomponenter på ett lager-för-lager-sätt. Höghållfasta nickelbaserade superlegeringar lider dock alltid av sprickbildning i processen under AM-processen, vilket knappt elimineras av processoptimeringen. Rätt blandning av elementen hjälper till att minska känsligheten för sprickbildning. Genom att förstärka både värme- och deformationsbeständigheten i de känsliga områdena genom tillägg av skraddarsydda legeringselement, uppvisar den nickelbaserade superlegeringen högre sprickningsbeständig kapacitet. En kemisk sammansättningsbaserad modell föreslogs baserad på detta koncept för att förutsäga sprickningskänsligheten under AM. Baserat på denna modell har två nya superlegeringar anpassade för AM-process marknadsförts. Undersökta av drag-, kryp- och oxidationsegenskaperna vid hög temperatur visar de nya legeringarna några överlägsna prestanda jämfört med de traditionella superlegeringskvaliteterna. Ett steg längre har behandlingar efter AM-bearbetning visat sig ha en betydande inverkan på mekanisk prestanda.

Detta examensarbete fokuserar på relationerna kemi/mikrostruktur/egenskaper hos nickelbaserad superlegering genom AM-processer. Legeringsdesignmetoden i denna studie ger en ny metod för att hantera sprickbildningsproblemen hos dessa legeringar av AM.

Dessutom bidrar de egenskapsresultat som visas i denna studie till att komplettera materialdatabasen.

Popular Science Summary

Approximately 13.8 billion years ago, right after the Big Bang, the lightest elements: Hydrogen, Helium, and a small amount of Lithium, were produced. Larger-mass elements up to Iron were forged later by nuclear fusion in the hearts of stars and in supernova. The heavier elements than Iron like Cobalt and Nickel and so on were born by the neutron stars merging. The mixture of different elements creates every possibility on this planet.

A nickel-based superalloy is a big reservoir of a mixture of types of elements. This alloy is widely used as the critical component material in high-temperature operation environments. Multiple benefits of the selection of Nickel as the major element can be found. For example, Nickel has a relatively high melting temperature (1455 °C) ensures the intrinsic high-temperature capacity, compared with for example Magnesium (650 °C) and Aluminium (660 °C). Nickel does not have solid-state phase transformation at the operating temperatures, compared with for example Titanium (HCP to BCC) and Iron (BCC to FCC to BCC). Nickel has an FCC crystal structure which is generally more ductile than other types of crystals. Nickel is a good solvent for alloying elements. The combination of elements in this alloy also matters a lot. For example, the addition of elements like Aluminium and Titanium assists the formation of the intermetallic compounds for improved high-temperature strength. The addition of refractory elements like Tungsten and Molybdenum improves the high-temperature deformation resistance. The addition of low-mass elements like Carbon and Boron strengthens the grain boundaries of these materials.

The recent rapidly developing additive manufacturing (AM), also known as three-dimensional (3D) printing offers a unique manufacturing process for producing metallic components in a layer-by-layer manner. However, high-strength nickel-based superalloys always suffer from in-process cracking during the AM process, which cannot be eliminated by the process optimization. The right mixture of the elements helps reduce the cracking susceptibility. By reinforcing both heat and deformation resistance of the vulnerable regions via the addition of tailored alloying elements, the nickel-based superalloy show higher cracking resistant capacity. A chemical composition-based model was proposed based on this concept to predict the cracking susceptibility during AM. Based on this model, two new superalloys adapted for AM process have been promoted. Examined by the high-temperature tensile, creep, and oxidation properties, the new alloys show some superior performances to the heritage superalloy grades. A step further, post-AM-processing treatments have been shown to have a significant influence on mechanical performances.

This thesis focuses on the chemistry/microstructure/properties relations of nickel-based superalloy by AM processes. The alloy design approach in this study provides a new method to cope with the cracking issues of these alloys by AM. In addition, the property results demonstrated in this study contribute to supplementing the materials database.

Acknowledgments

This research is financially supported by the Swedish Governmental Agency for Innovation Systems (Sveriges innovationsmyndighet, Vinnova) MADAM (grant 2018-00804), MAGDA (grant 2021-01005) projects, and the Vinnova Competence Center for Additive Manufacturing – metal (CAM²). I would also like to acknowledge the organizations for providing me with travel funds, that is Agora Materiae Graduate School for multidisciplinary PhD students at Linköping University, and Stiftelsen Axel Hultgren.

It has been a pleasant and joyful journey since September 2018 as a PhD student at Division of Engineering Materials (KMAT), Department of Management and Engineering (IEI), Linköping University (LiU), Sweden. Foremost, I would like to thank my main supervisor, Prof. Johan Moverare, who offered me this great opportunity to dive into this interesting PhD project. I appreciate the immense coaching and mentoring you gave me. I also appreciate your support of my self-development and decision-making. I would like to thank my co-supervisor, Prof. Ru Lin Peng, for your valuable remarks and helpful inputs. Thank you both my supervisors, and your contagious passion for research which always encourages me to explore deeper. I also really appreciate my supervisors for offering me flexible spaces and 'tolerating' my insane thoughts and imaginations to explore the metallurgy field.

Special gratitude goes to Dr. Hans Gruber and Dr. Fiona Schulz from Chalmers University of Technology/CAM², for printing the studied LPBF samples and for the close collaboration. I would like to appreciate my other project partners, Prof. E. Hryha from Chalmers University of Technology, Dr. H. Brodin from Siemens Energy AB, Dr. S. Bengtsson from Höganäs AB, K. Minet and A. Shaikh from EOS Finland Oy, Dr. A. Eklund and J. Gårdstam from Quintus Technologies AB for the fruitful and helpful discussions on this project and the efforts on making the new materials. I would like to thank my collaborators, Dr. V. Luzin from ANSTO for the neutron diffraction measurements, Dr. R. Boyd from IFM, LiU for TEM assistance, Dr. T. Ma and Dr. S. Hosseini from RISE for the LPBF IN718 publication, Dr. O. Adegoke from University West for the LPBF CM247LC publication, Dr. P. Kontis from Max-Planck-Institut für Eisenforschung and Norwegian University of Science and Technology for the Atom Probe Tomograph experiments, Dr. Y. Tang from University of Oxford for the tensile testing on LPBF MAD542, Dr. Z. Chen from Chalmers University of Technology, Dr. M. Neikter from University West, and Dr. R. Woracek from European Spallation Source for the ongoing collaboration on LPBF IN718, Dr. T. Fritsch and Dr. S.M. Itziar from BAM for the Micro Computed Tomography measurements.

I am very grateful to work with all my colleagues at KMAT, LiU. Thank you all for creating this wonderful working environment. Thank you Ingmari, our administrator, for taking care of every detailed administration works excellently. I wish you a happy retirement this Spring! Thank you, Rodger and Patrik, for your technical supports, without you my characterization and mechanical testing works could not be carried out that smoothly. I

would like to thank you my fellow peers (and alumni), Dunyong, Pimin, Hank, Prabhat, Pavel and so on, I really enjoyed the inspiring discussions with you guys.

I would like to deeply thank my family and family in law for the kind support and understand of me. A huge acknowledgment and love express to my wife, Yao (瑶), for your love and support. Life goes low, life goes high, thank your love always go with me.

A handwritten signature in black ink that reads "Jinghao Xu". The signature is written in a cursive, flowing style.

Linköping, March 2022

List of Publications

Publications appended in this thesis

Paper I

J. Xu, H. Gruber, D. Deng, R.L. Peng, J.J. Moverare, Short-term creep behavior of an additive manufactured non-weldable Nickel-base superalloy evaluated by slow strain rate testing, *Acta Mater.* 179 (2019) 142–157.

Contribution: Performed the microstructure and fractography characterizations, data analysis, mathematic formulating, and manuscript writing and revising.

Paper II

J. Xu, H. Gruber, R. Lin Peng, J. Moverare, A Novel γ' -Strengthened Nickel-Based Superalloy for Laser Powder Bed Fusion, *Materials (Basel)*. 13 (2020) 4930.

Contribution: Performed the microstructure characterizations, chemistry measurements, data analysis, manuscript writing, and revising.

Paper III

J. Xu, H. Brodin, R.L. Peng, V. Luzin, J. Moverare, Effect of heat treatment temperature on the microstructural evolution of CM247LC superalloy by laser powder bed fusion, *Mater. Charact.* (2022) 111742.

Contribution: Performed the microstructure characterizations, data analysis, mathematic formulating, and manuscript writing.

Manuscript IV

J. Xu, P. Kontis, R. Peng, J. Moverare, Modelling of Additive Manufacturability of Nickel-Based Superalloys for Laser Powder Bed Fusion, Submitted to a journal.

Contribution: Proposed the concept, performed the SEM and EBSD characterization, data analysis, mathematic formulating, and manuscript writing and revising.

Manuscript V

J. Xu et al. On the role of minor elements in the additive manufacturability and high-temperature mechanical property of laser powder bed fused IN738LC superalloys, in manuscript.

Contribution: Performed the slow strain rate tensile testing, microstructure and fractography characterizations, data analysis, mathematic formulating, and manuscript writing.

Manuscript VI

J. Xu et al. Tailoring high-temperature mechanical properties of a novel laser powder bed fused nickel-based superalloy by post-processing treatments, in manuscript.

Contribution: Performed the microstructure and fractography characterizations, neutron data analysis, post EBSD analysis, manuscript writing.

Manuscript VII

J. Xu et al. A crack-resistant superalloy for 3D printing: creep performance and oxidation properties, in manuscript.

Contribution: Performed the tensile, creep, and oxidation testing, conducted differential scanning calorimetry measurement, analyzed neutron texture data, characterized microstructures, wrote manuscript.

Summary of appended papers/manuscript:

In manuscript IV, a two-parameter-based heat resistance and deformation resistance (HR-DR) model is proposed to predict the cracking susceptibility of nickel-based superalloys based on their chemical compositions. This HR-DR model successfully predicts the additive manufacturability of superalloys, validated by the experimental data. In paper II, with help of the HR-DR model, a new superalloy MAD542 adapted to the LPBF process is proposed. This alloy is crack-resistant.

In papers I and V, the studied materials are laser powder bed fused (LPBF) IN738LC superalloy. In paper I, the high-temperature short-term creep properties and the time-dependent deformation mechanism of polycrystalline LPBF superalloy are discussed. At the operation condition at elevated temperatures, for example, at 850 °C, grain boundary sliding is the controlling aspect that dominates the creep deformation. In paper V, the influence of minor elements addition such as B and Zr on the cracking susceptibility during the LPBF process is investigated. The cracking susceptibility of IN738LC derivatives with various B and Zr concentrations is quantitatively predicted by the HR-DR model. The low-B and low-Zr composition show the largest process window, while ductility and deformation-resistant are slightly reduced owing to the lack of grain boundary strengthening effect from these minor elements.

Paper III and VI present the influence of post-processing treatments on the grain structure and mechanical properties of high-strength nickel-based superalloys, CM247LC and MAD542 respectively. The super- γ' -solvus temperature is the key to promoting recrystallization in γ' -strengthened LPBF superalloys, thus, the crystallographic texture is accordingly reduced. However, the recrystallized microstructure worsens the high-temperature mechanical properties in terms of reduced ductility by increasing the intergranular fracture sensitivity.

Manuscript VII demonstrates the new superalloy named Alloy738+ adapted for the LPBF process. The composition of Alloy738+ was modified based on the parent superalloy IN738LC for casting, with aiming at the improved printability. In this manuscript, the alloy development approach, creep and oxidation properties were reported.

All the appended papers/manuscripts are focusing on the γ' -strengthened nickel-based superalloy and the corresponding LPBF process. The contents are diverted to materials development, microstructural characterization, and mechanical property examination, where the established knowledge and understanding did help on the PhD projects from different perspectives.

Publications not included in this thesis

Paper VIII

J. Xu, H. Gruber, R. Boyd, S. Jiang, R.L. Peng, J.J. Moverare, On the strengthening and embrittlement mechanisms of an additively manufactured Nickel-base superalloy, *Materialia*. 10 (2020) 100657.

Contribution: Performed microstructure and fractography characterizations, data analysis, mathematic formulating, and manuscript writing and revising

Paper IX

J. Xu, F. Schulz, R.L. Peng, E. Hryha, J. Moverare, Effect of heat treatment on the microstructure characteristics and microhardness of a novel γ' nickel-based superalloy by laser powder bed fusion, *Results Mater.* 12 (2021) 100232.

Contribution: Proposed the concept, designed the experiments, operated the characterizations, analyzed results, wrote, and revised manuscript.

Paper X

J. Xu, T. Ma, R.L. Peng, S. Hosseini, Effect of post-processes on the microstructure and mechanical properties of laser powder bed fused IN718 superalloy, *Addit. Manuf.* 48 (2021)

Contribution: Operated the transmission electron microscopy characterizations, analyzed results, wrote, and revised manuscript.

Paper XI

H. Wärner, J. Xu, G. Chai, J. Moverare, M. Calmunger, Microstructural evolution during high temperature dwell-fatigue of austenitic stainless steels, *Int. J. Fatigue.* (2020) 105990.

Contribution: Operated the transmission electron microscopy characterizations.

Paper XII

L. Cui, S. Jiang, J. Xu, R. Peng, R. Mousavian, J. Moverare, Revealing relationships between microstructure and hardening nature of additively manufactured 316L stainless steel, Mater. Des. 198 (2021).

Contribution: Operated the transmission electron microscopy characterizations.

Paper XIII

O. Adegoke, S.R. Poliseti, J. Xu, J. Andersson, H. Brodin, R. Pederson, P. Harlin, Influence of laser powder bed fusion process parameters on the microstructure of solution heat-treated nickel-based superalloy Alloy 247LC, Mater. Charact. 183 (2022) 111612.

Contribution: Operated differential scanning calorimetry measurements.

List of Abbreviations

3D	Three-dimensional
AM	Additive Manufacturing
APB	Anti-phase Boundary
ASME	American Society of Mechanical Engineers
BCT	Body-Centered Tetragonal
BD	Building Direction
BSE	Backscattered Electron
BTR	Brittle Temperature Range
CSI	Crack Susceptibility Index
DC	Dendrite Core
DDC	Ductility-Dig Cracking
DMLM	Direct Metal Laser Melting
DMLS	Direct Metal Laser Sintering
DoE	Design of Experiment
DS	Directional Solidification
EBM	Electron Beam Melting
EB-PBF	Electron Beam Powder Bed Fusion
EBS	Electron Backscatter Diffraction
EDS	Energy Dispersive X-ray Spectroscopy
FCC	Face-Centered Cubic
FE-SEM	Field Emission Scanning Electron Microscope
GB	Grain Boundary
HB	Horizontally Built
HCS	Hot Cracking Sensitivity
HIP	Hot Isostatic Pressing
HR-DR	Heat Resistance-Deformation Resistance
HT	Heat Treatment
ID	Interdendritic region
ISO	International Organization for Standardization
LMF	Laser Metal Fusion
LMP	Larson Miller Parameter
LPBF	Laser Powder Bed Fusion
MGB	Migrated Grain Boundary
M.R.D	Multiples of a Random Distribution

NIMS	National Institute for Materials Science
OM	Optical Microscopy
PM	Powder Metallurgy
PMZ	Partially Melted Zone
PPM	Parts Per Million
RS	Residual Stress
SAC	Strain-Age Cracking
SE	Secondary Electron
SGB	Solidification Grain Boundary
SIBM	Strain Induced Boundary Migration
SLM	Selective Laser Melting
SSRT	Slow Strain Rate Tensile
SX	Single Crystal
TB	Twin Boundary
TCP	Topologically Close-Packed
TEM	Transmission Electron Microscopy
TGM	Temperature Gradient Mechanism
TSR	Thermal Shock Resistance
TTT	Time-temperature-transformation
VB	Vertically built
WDS	Wavelength Dispersive X-ray Spectroscopy

Nomenclature

ΔT_b	Undercooling to approaching coalescence
$\Delta \Gamma_b$	Energy difference of liquid/solid and grain boundary interfaces
δ	Thickness of an isolated solid-liquid interface
ΔS_f	Entropy of fusion
γ_{gb}	Grain boundary energy
γ_{sl}	Solid/liquid interfacial energy
τ_{oro}	Orowan shear stress
τ_{cut}	Shear stress required for dislocation cutting
G	Shear modulus
b	Magnitude of Burger's vector
$L_{\gamma'-\gamma'}$	Spacing between γ' particles
$d_{\gamma'}$	Average size of precipitates
γ_{APB}	Anti-phase boundary energy
$d\gamma$	Unit shear strain
ρ	Dislocation density
l	Average length of dislocation
$\alpha_{Tay.}$	Materials constant for Taylor's strengthening
M	Taylor's factor
M_{creep}	Merit index for creep resistance
x_i	Atomic fraction of solute i
\bar{D}_i	Appropriate interdiffusion coefficient
T	Absolute temperature in Kelvin
c_{LM}	Larson-Miller constant
t	Time
χ	Crack susceptibility index
σ_{UTS}	Ultimate tensile strength
σ_T	Thermal stress
f_s	Fraction solid
E	Energy density of laser powder bed fusion
P	Laser power
V_s	Scan speed
H	Hatching distance
L	Layer thickness
P_V	Total input power per unit volume

$\dot{\epsilon}$	Strain rate
K_p	Parabolic rate constant

Contents

Chapter 1 General introduction	1
1.1 Research background	1
1.2 Research objectives	2
Chapter 2 Literature review	3
2.1 Laser powder bed fusion	3
2.1.1 LPBF process	3
2.1.2 LPBF application	4
2.2 Post-AM-processing treatments	4
2.2.1 Hot Isostatic Pressing	4
2.2.2 Heat treatment	5
2.3 Challenges in the LPBF process	7
2.3.1 Residual stresses	7
2.3.2 Porosity	7
2.3.3 Process induced cracking	8
2.3.3.1 Solidification cracking	8
2.3.3.2 Liquation cracking	10
2.3.4 Anisotropic behavior	10
2.4 Challenging parts in post-process treatment	11
2.4.1 Sluggish recrystallization	11
2.4.2 Post-process treatment-induced cracking	12
2.4.2.1 Strain-age cracking	12
2.4.2.2 Ductility-dip cracking	12
2.5 History and development of nickel-based superalloys	12
2.5.1 Development of alloy composition	12
2.5.2 Development of manufacturing processes	13
2.6 Physical metallurgy of nickel-based superalloy	15
2.6.1 Phases and microstructures	15
2.6.2 Alloying elements effects	16

2.6.3 Strengthening mechanisms.....	18
2.6.3.1 Solid solution strengthening.....	18
2.6.3.2 Precipitation strengthening.....	18
2.6.3.3 Grain boundary strengthening	19
2.6.3.4 Dislocation strengthening	19
2.7 Creep in nickel-based superalloys	20
2.7.1 Creep mechanisms	20
2.7.2 Creep performance of LPBF processed superalloys	20
2.8 Chapter summary.....	22
Chapter 3 Experimental methodology	23
3.1 Materials.....	23
3.2 LPBF process.....	24
3.3 Metallographic preparation	25
3.4 Optical microscopy.....	25
3.5 Electron microscopy.....	25
3.5.1 Scanning electron microscopy	25
3.5.2 Electron backscatter diffraction	25
3.5.3 Transmission electron microscopy	25
3.6 Etching	26
3.6.1 Chemical etching.....	26
3.6.2 Electro-etching.....	26
3.7 Mechanical testing	26
3.7.1 Tensile testing at room temperature	26
3.7.2 Slow strain rate tensile testing.....	27
3.7.3 Creep testing	27
3.8 Oxidation testing	27
Chapter 4 Crack susceptibility model	29
4.1 Cracking behavior of nickel-based superalloy in LPBF	30
4.2 Concept of HR-DR model	33
4.3 Additive manufacturability diagram	34

4.4 Validation of HR-DR model	36
Chapter 5 LPBF and Post-processing	37
5.1 LPBF manufacturing of MAD542 and Alloy738+	37
5.2 Grain structure evolution	38
5.3 Effect of post-processing on the precipitates	40
Chapter 6 Mechanical properties	41
6.1 Room-temperature tensile properties	42
6.2 High-temperature tensile properties	44
6.3 High-temperature slow strain rate tensile testing	46
6.4 Correction between SSRT and creep	46
6.5 Creep property of LPBF superalloys	47
6.6 Summarized time-dependent performance.....	50
Chapter 7 Oxidation property	53
Chapter 8 Conclusions and outlook.....	55
8.1 Conclusions	55
8.2 Outlook	57
Bibliography	58

Chapter 1 General introduction

This dissertation includes the research results by the author Jinghao Xu from his PhD study since September of 2018 at the Division of Engineering Materials in Linköping University, Sweden. The form of this thesis is a comprehensive summary.

1.1 Research background

Precipitation-strengthened nickel-based superalloys have extraordinary mechanical properties at high temperatures, oxidation and corrosion resistance, and outstanding phase stability, allowing the implementation of these materials for the critical hot-section components. Different from the conventional manufacturing methods, based on the layer-by-layer manner of manufacturing, additive manufacturing (AM), also known as three-dimensional (3D) printing, provides huge opportunities to fabricate complicated components owing to its high design flexibility.

Until recently, the largest portion of the investigations in the AM community has been conducted on commercial weldable superalloys, such as Inconel 718, Inconel 625, and Hastelloy X. On the other hand, owing to the excellent high-temperature chemical and mechanical properties and serviceability of γ' -strengthened superalloys, the production of them by the AM process has always been a great vision of the AM community. The AM-processing of γ' -strengthened superalloys, however, represents a significant difficulty due to their high crack susceptibility during AM and/or post-processing. It is critical to establish a strong link between the chemical composition-related materials index and additive manufacturability.

In this study, the alloy development is targeting at proposing the new superalloys adapted to the AM processing, which present high cracking-resistance during the AM process, and meanwhile, maintain the great creep and oxidation resistance.

1.2 Research objectives

In this PhD dissertation, the investigations focus on the chemistry, processing, structure, and property of LPBF manufactured high-performance nickel-based superalloys. A novel γ' -strengthened nickel-based superalloy and a modified superalloy have been designed for the LPBF process. Both of the superalloys are aiming at good high-temperature mechanical performance, especially creep resistance and oxidation resistance. Other heritage grades of γ' -strengthened superalloys and their derivatives including IN738LC and CM247LC fabricated by LPBF process are investigated by microstructural characterization and mechanical property examinations.

The primary objectives of this work are:

1. To understand the in-process cracking mechanisms for high-strength nickel-based superalloys during the LPBF process. To propose a reliable and easy-to-use cracking susceptibility model for this group of alloys. To propose new superalloys chemical compositions based on additive manufacturability and high-temperature performance indices.

2. To understand the microstructural evolution of high-strength nickel-based superalloys during the post-AM-treatments. To tailor the high-temperature mechanical properties by post-processing design.

3. To examine the creep and oxidation properties of LPBF high-strength nickel-based superalloys. To understand the influence of minor elements addition on the time-dependent high-temperature deformation behaviors.

Chapter 2 Literature review

2.1 Laser powder bed fusion

Seven processes including binder jetting; directed energy deposition; material extrusion; material jetting; powder bed fusion; sheet lamination; vat photopolymerization, are defined as the additive manufacturing categories, according to the International Organization for Standardization (ISO) / ASTM [1]. Plastics, metallics, organics, and ceramics are the most widely adapted materials for AM processes [2]. One of the most important subcategories of powder bed fusion is LPBF, which is commonly used to fabricate metallic materials. There are several other terminologies with different naming systems that refer to the same process, such as selective laser melting (SLM) [3], direct metal laser sintering (DMLS) [4], LaserCUSING [5], laser metal fusion (LMF) [6], and direct metal laser melting (DMLM) [7], most of which are based on the trademarks of the printing system manufacturers. The energy source for melting the powder bed in LPBF is a laser beam. Another popular powder bed fusion process is electron beam powder bed fusion (EB-PBF), also known as electron beam melting (EBM) [8], which has an electron beam as the energy source.

2.1.1 LPBF process

Although the LPBF processes have been given different names, the key features of the LPBF process are the laser beam as the thermal source for melting the particles in the powder bed, as discussed previously. As seen in schematic illustration in Fig. 2.1. Besides the powder-bed chamber, a dispenser bin serves as the powder reservoir. The LPBF process starts on distributing the powders on the build platform, which is the work area for the layer-by-layer melting. The build platform moves down, and the recoater blade moves back and forth to fill another layer of powders after selective laser fusion of each layer.

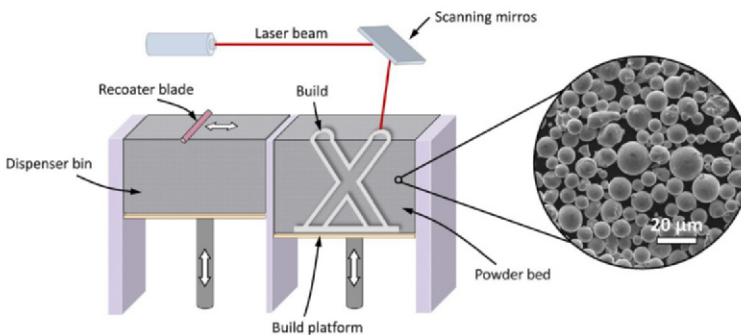


Fig. 2.1. Schematic illustration of the LPBF system.

The powders used for LPBF typically range in size from 20 to 50 μm . Pre-alloyed powders, having the alloying elements doped before the power supply, are commonly utilized to fabricate the component. The build speed of LPBF could be boosted because of the mechanical movement of scanning mirrors. Furthermore, several scanning procedures can be implemented, which have a significant impact on process defects, microstructure, crystallographic anisotropic behavior, surface roughness, and residual stresses [9]. The LPBF process is commonly carried out in a protective atmosphere using inert gas [10], such as N_2 , Ar, or even He (Helium) [11], to reduce the oxidation attack.

2.1.2 LPBF application

The component and their application condition are largely dependent on which type of materials have been fabricated and how their serviceability perform. The nickel-based superalloys are the focus of this research, it is designed to survive the severe service environment at high temperatures. Obviously, the design flexibility of components subjected to high temperatures is critical, for example, a more complex internal cooling system for gas turbine parts aids in the reduction of combustion emissions. The LPBF-processed nickel-based superalloy might likely be advantageous in this regard, which can barely be manufactured by the conventional routes. For example, General Electric Company filed the patent, regarding the fuel nozzle part processed with a batch of AM techniques including LPBF for a gas turbine engine in March 2015 [12]. In 2017, SIEMENS was awarded for the achievement of the first successfully 3D-Printed gas turbine blades, which are tested in a demanding working temperature higher than 1250 $^{\circ}\text{C}$ according to the American Society of Mechanical Engineers (ASME) [13].

2.2 Post-AM-processing treatments

Here, the post-AM-processing treatments indicate the treatments (usually at elevated temperatures) which are necessarily applied after the printing of the part. Post-AM-processing treatments are the key to improving the component integrity and mechanical performances.

2.2.1 Hot Isostatic Pressing

Hot isostatic pressing (HIP), as a primary materials shaping process, has been developed before the 1960s [14]. The material exposed to the HIP is treated under both high temperatures and high isostatic pressures. The use of inert gas as a pressure-transmitting medium to apply three-dimensional equivalent pressure distinguishes the HIP process from other materials manufacturing procedures. As a result, HIP frequently supplies near-net-shape components.

Typically, two kinds of materials are subjected to HIP: the powders, and the pre-shaped part. One of the most important applications for the HIP is powder metallurgical turbine

discs composed of nickel-based superalloys. Pre-alloyed powders that are sealed in the can condense under high temperature/pressure to manufacture the powder metallurgical part using HIP. Other thermomechanical techniques, including hot extrusion and isothermal forging, can be used to fabricate near-net-shape turbine discs after HIP. In addition, before service, HIP is commonly used to cure flaws in Ti alloys and superalloys castings. The HIP is also used to rejuvenate components that have been retired, owing to the microstructure evolution and localized chemistry changes thanks to the coupled high temperature and pressure. For example, after HIP, the degraded microstructure served in long-term rejuvenates owing to the homogenization of dendrite microstructure [15]. It demonstrated that rejuvenating effects introduced by HIP not only heal the defects but also reset dislocation densities, then further improve the creep resistance of a deformed superalloy [16].

Because as-AM-processed products are prone to have internal metallurgical defects, HIP is a necessary step in ensuring that the parts are of greater quality. For γ' -strengthened nickel-based superalloys, HIP effectively acts as the approach in healing the in-process-induced cracks [17]. The commonly implemented HIP pressure is in the range of 1000-2000 bar (100-200 MPa), while the HIP temperature varies according to mainly the γ' solvus temperature of the specific superalloy. For example, above the super-solvus temperature, the creep deformation occurs under the single austenite condition of nickel-based superalloys, where plastic flow also happens since the HIP pressure exceeds the yield strength at the HIP temperature. Although the super-solvus HIP exhibits good crack-healing, recrystallization response, and reducing crystallographic anisotropy, the expense is significant grain growth. To maintain the fine grain structure, HIP could be conducted at the sub-solvus temperature, in which the γ' would not fully be dissolved, and then pin the grain boundary (GB) migration and prevent the dramatic grain growth [18].

The HIP cycle is more and more frequently used for the LPBF processed nickel-based superalloy, where the prioritized purpose is to heal the internal microcrack introduced during the printing process. According to the pioneering research by Carter et al. [19], the internal cracks of LPBF processed CM247LC superalloy are effectively healed by HIP, while the surface-connected cracks remain.

2.2.2 Heat treatment

The 'difficult-to-weld' property of γ' -strengthened nickel-based superalloys, and therefore the necessity for crack healing, make the HIP one of the post-AM-process routes for them. The HIP is not usually required for nickel-base superalloys with good additive manufacturability.

Heat treatment (HT) plays a pivotal role in tuning the alloying element distribution and tailoring the microstructures. Conducting HT in γ' -strengthened nickel-based superalloys serves for multiple objectives:

- 1) to achieve chemical homogeneity, promote recrystallization/grain growth, and develop precipitates, which is usually completed by solutioning treatment.

2) to further modify the morphology, distribution, and volume fraction of the γ' precipitates, which is usually referred as aging treatment.

Owing to the far different pristine microstructure introduced by AM process compared to the conventional manufacturing processes, the HT scenarios for AM superalloys are normally modified accordingly. Firstly, the solidification dendritic arm spacing in the as-built condition is restricted to sub-micron for LPBF and several micrometers for EB-PBF because of the relatively high cooling rate of the AM process. The solutioning treatment for highly alloyed material systems, such as a nickel-based superalloy with a large number of refractory elements added, is challenging. For example, the solution treatment of advanced single crystal superalloy requires well-designed heating profiles with a variant combination of temperature step and dwell time, in order to, on the one hand, dissolve the γ/γ' eutectic phases and accelerate the chemical homogenization, and on the other hand, avoid the occurring of incipient melting at the lower solidus region caused by the segregation of alloying elements [20,21]. However, the fine dendrites of the AM microstructure are beneficial for shortening the solutioning treatment.

By Ramsperger et al. [22], the solutioning treatment for EB-PBF processed CMSX-4 superalloy may become easier compared to its casting counterpart. From the heating perspective, no extra heating ramps are necessary, and no incipient melting will be induced. Second, complete chemical homogenization may be achieved in a couple of minutes, whereas cast CMSX-4 takes several hours. These advantages are attributed to the significantly finer dendritic structure in the EB-PBF alloy, leading to the elemental segregation being only constrained into the micrometer scale [23]. The finer dendrite arm spacing results in a shorter diffusion distance.

It is worth highlighting here, although the γ' precipitation was highly suppressed in the LPBF process, extensive γ' forms during heat treatment and/or HIP. The γ' in superalloy is known to have the fast precipitation kinetics. For example, 0.5% γ' form within 1s and 2s in CM247LC and IN738LC superalloys respectively at the corresponding 'nose' temperature from the modeled time-temperature-transformation (TTT) diagrams [24]. The un-released residual stress induced by the LPBF process plus the precipitation stress largely increase macro-cracking susceptibility. However, the macro-cracking behavior of high- γ' -volume LPBF superalloys during the post-processing treatment is barely reported or well-understood from the literature, unfortunately.

2.3 Challenges in the LPBF process

Several important features of the LPBF process may be regarded as problematic characteristics, as they either diminish component integrity or compromise mechanical performance.

2.3.1 Residual stresses

The stresses that remain inside a solid material when no external forces are applied are known as residual stresses (RS). The relatively high value of RS is generally developed in the AM parts owing to its extremely large temperature gradient during printing, which leads to the detrimental effect of the component integrity via geometrical distortions or cracking [25].

According to different dimensional scales of RS, three types of RS can be categorized: 1) Type I RS, which occurs at the size that is comparable to the bulk materials dimensions in macro-scale; 2) Type II RS, which occurs at the crystal and phase scales restricted into the micro size; 3) Type III RS, which occurs at the atomic scale and is related with the crystal defects. Commonly, type II and type III are named as micro-stress [26]. While in AM processed part, the type I RS is the key to controlling the component integrity. To interpret the underlying mechanisms of the type I RS generalization in LPBF, Mercelis and Kruth [27] proposed the temperature gradient mechanism (TGM): a steep temperature gradient close to the laser beam region is obtained, owing to the rapid heating of the upper surface plus the slow heat conduction. The strength of the materials decreases as the temperature increases. The possible plastic deformation can be introduced if the RS exceeds the elastic limit at the 'hot' region. The compressive and tensile RS are developed during the heating and cooling respectively. Owing to the related laser process, i.e., during the heating process, the underlying material with lower temperature constricts the thermal expansion of the heated top layer, introducing the compressive strain, while during the cooling process, the underlying material constricts the shrinkage of the top layer, leading to a developed tensile strain.

2.3.2 Porosity

Porosity is a group of pore-like defects within the internal volume of the material which is commonly observed in the AM processed parts. The porosity defects can be the detrimental source to reduce the mechanical properties, by acting as the potential crack initiation sites, which may lead to premature failure [28]. Based on the dimensional scale, the porosity could be then sub-categorized into two types: the metallurgical pores and keyhole pores. Regarding the origin of metallurgical pores, it is generally accepted as the aggregation of entrapped gases [29]. In contrast, the formation of keyhole pores is caused by insufficient melt overlapping. For example, Xiao et al. [30] attributed the keyhole pores to the incomplete filling of the gaps with the molten materials, which is largely dependent on the print parameters. Furthermore, the lack of fusion is attributed to not only the un-

optimized printing parameters but also the nature of the printed materials. For example, Al alloys generally show higher susceptibility to the keyhole pores because of the higher affinity between the Al and the oxygen in the build chamber, where the formed oxide potentially acts as the initial site for keyhole pores [31]. From the morphology and size wise, the metallurgical pores are usually shaped spherical with the diameter generally less than 100 μm , in contrast, the keyhole-like pores are in irregular shape and commonly have a size greater than 100 μm . However, in the LPBF nickel-based superalloy, the keyhole-like porosity can be effectively reduced by modifying the processing window. In the early study (the year of 2013) of LPBF of IN738LC superalloy by Rickenbacher et al. [32], by optimizing the printing process parameters, this kind of porosity could be dramatically reduced from over 50% to less than 0.5%.

2.3.3 Process induced cracking

High-strength nickel-based superalloys are very susceptible to AM process cracking, which hinders further development. Two types of in-process cracking are introduced in this section: solidification and liquation cracking.

2.3.3.1 Solidification cracking

Solidification is a crucial aspect of the AM process, from powders to bulk materials. Solidification cracking, also known as hot tearing or hot cracking, appears during the solidification process [33]. Extensive research in the field of casting and welding [34,35], has tried to interpret the underlying mechanisms. Solidification cracking appears in the melt pool during the AM process, where it reflects the formation of irreversible failure in a partially solid state. Generally, the mechanism of solidification cracking is accepted as the combination of impeded compensation by liquid flow with thermal stresses during the solidification shrinkage [33]. Like other cracking mechanisms, solidification cracking comprises two main processes, crack initiation, and propagation. It can be summarized from many pieces of research [36,37] that the solidification cracking initiates above the solidus temperature where liquid is still partly existed, and then propagate along with the interdendritic liquid film, where the liquid phase barely has any stress-bearing capacity. In particular, because the insufficient liquid flow cannot well compensate for the solidification shrinkage, cavities of pores are prone to form [38]. Then micro-cracks are prone to initiate at these defects. In addition, the rapid solidification process results in strong thermal gradients which leads to thermal contraction, acting as the driving force for solidification crack propagation [39].

As mentioned above, the mushy zone is the critical microstructure initiating solidification cracking. However, misunderstanding may take place regarding the slurry and mush, where both zones are in the state of semisolid. To distinguish them, the difference is that in the slurry zone, the newly formed grains are suspended freely in the liquid flow, while in mush zone, the grains are interacted and tangled with each other. Several models [39,40] refer that the extended mushy zone will suffer more solidification shrinkage strain and

result in higher solidification cracking susceptibility. From the thermodynamic perspective, the solidification range can then be referred as a brittle temperature range (BTR), which is defined as the difference value between liquidus and solidus temperature [41]. Flemings [42] concluded that a narrow solidification range leads to a nearly uniform mush. The mushy zone can be estimated as the solidification temperature range divided by the thermal gradient in a length dimension [42]. Shankar [43] reported that, in 304L stainless steels, crack density increased from 0.1 mm/mm² to 1.1 mm/mm² with the BTR increasing from 21 °C to 68 °C.

It can be concluded that the reduced size of the mushy zone is beneficial to reduce the solidification cracking susceptibility. One effective way to reduce the mushy zone size is to decrease the solidification range, which requires the reduction of the temperature difference between liquidus to solidus. The solidus temperature largely depends on the eutectic reaction point. However, segregation of impurities lowers solidus temperature by forming eutectic phases, which is deleterious to solidification cracking resistance [44]. For example, sulfur in steel drastically lowers the solidus from 1365 °C to 988 °C [45,46] as the formation of low melting Fe-S eutectic films along the interdendritic and grain-boundary regions [47]. Another important approach for the reduction of the mushy zone is targeting on modifying the solidification procedure, e.g., to increase the thermal gradient. Goodwin suggested [44] that increasing heat input (low thermal gradient) increases the susceptibility of cracking in the welding of 316 stainless steel.

Referring to solidification cracking, it is inevitably worth mentioning the theoretical model, which correlates the solidification microstructure with the grain structure, developed by Michel Rappaz. At the last stage of solidification, grain boundary shows critical influence on the solidification cracking, where the grain boundary coalescence improves the intergranular strength of solidifying dendritic structure to resist solidification crack [48]. Rappaz [49,50] supposed that planar liquid/solid interface coalescence to a grain boundary can be described by the following equation.

$$\Delta T_b = \frac{\Delta \Gamma_b}{\delta} = \frac{\gamma_{gb} - 2\gamma_{sl}}{\Delta s_f} \frac{1}{\delta} \quad (2.1)$$

Where ΔT_b is an undercooling to approaching coalescence, $\Delta \Gamma_b$ is the difference between the two energies (γ_{gb} and γ_{sl}), δ is the thickness of an isolated solid-liquid interface, Δs_f is the entropy of fusion. It is worth noting that coalescence mainly is determined by the difference between grain boundary energy, γ_{gb} and twice the solid/liquid interfacial energy, $2\gamma_{sl}$, which determines the ‘attractive’ and ‘repulsive’ behavior of boundaries. When $\gamma_{gb} - 2\gamma_{sl} < 0$, the unstable liquid film serves as a bridge between neighboring dendritic arms. In this case, due to the poor wetting, the bridging droplets resist strain, leading to a lower crack susceptibility. It is supported by experimental evidence in Borland’s [51] research on Al alloy, where poor wetting features with larger dihedral angles represent higher weldability. If $\gamma_{gb} - 2\gamma_{sl} = 0$, it refers to a ‘neutral’ state, which means coalescence can occur with no extra undercooling. However, if $\gamma_{gb} - 2\gamma_{sl} > 0$, the stable liquid film remains at lower temperature until the undercooling exceeds the corresponding critical value. The interfaces are ‘repulsive’ and prone to be cracked.

2.3.3.2 Liquation cracking

Different from solidification cracking occurrence in the fusion zone, liquation cracking occurs at a partially melted zone (PMZ) where the sites are a bit away from the melt pool [52]. From the crack morphology perspective, liquation cracking shows intergranular features but does not reveal any dendritic morphology [53]. Liquation cracks are typically short, ranging from a few micrometers to a few millimeters.

The formation of liquation cracks is considered as the semi-continuous liquid film along grain boundaries in PMZ that cannot hold the tensile stresses induced by thermal gradient [54]. The re-heating temperature that introduces PMZ is lower than the overall solidus temperature. However, as the existence of some low-melting eutectic phases in the interdendritic region, the re-heating temperature can be high enough to induce the liquation locally. In superalloy IN718, alloying elements Nb and Ti residually segregate at interdendritic regions to form a greater quantity of low-melting liquid [55]. Once the re-heating temperature exceeds the eutectic reaction temperature, liquation initiates. The formation of liquation in this PMZ is crucial to developing a liquation crack.

Pepe and Savage [56,57] proposed the well-known constitutional liquation, which means the local eutectic melting of secondary phase at temperatures above the eutectic temperature but below the solidus of the alloy. In nickel-based superalloy Udimet 700, Waspaloy, Hastelloy X, and IN718, the formation of constitutional liquation can interact with secondary phases of carbide or other intermetallic compounds and the matrix from the reference [56,58–62]. In nickel-based superalloys which have a high-volume fraction of γ' precipitates, constitutional liquation could be a well-contributing factor to liquation cracking. The constitutional liquation is the dominant mechanism for liquation cracking of LPBF superalloy with high- γ' -volume fraction. It has been reported that superalloy IN738 cracked on PMZ grain boundary along resolidified γ/γ' eutectic constituent from liquated γ' phase [63]. Furthermore, Shahsavari [64] provided microstructural evidence using XRD mapping to confirm that the liquid film formed from constitutional liquation causes liquation cracking in superalloy Rene 80 weldments.

2.3.4 Anisotropic behavior

Owing to the relatively uniform heat dissipation direction during the AM process, the preferred grain growth direction is strongly parallel to the solidification direction. As a consequence, the columnar-shaped grain structures are commonly found in the LPBF alloys. The crystallographic orientation is highly dependent on the printing strategy. For example, the $\langle 011 \rangle$ dominated grain orientation parallel to the building direction can be developed during the unidirectional long scans [65,66], while $\langle 001 \rangle$ texture is generally recognized from the rotated non-directional scans [67].

The resultant textures strongly influence the anisotropic mechanical properties. One of the most significant comparisons is from the identical material fabricated horizontally and vertically. For example, as reported by Yu et al. [68], the horizontally built LPBF

Hastelloy X superalloy shows slightly higher yield strength than the vertically built parts while the elongation is highly reduced under tensile testing at 700 °C.

2.4 Challenging parts in post-process treatment

Post-LPBF-process treatments play an essential role in modifying the microstructures and the resultant properties of the materials. However, several problematic phenomena are considered as challenging parts during post-processing.

2.4.1 Sluggish recrystallization

In this study, the sluggish recrystallization of LPBF superalloys is defined as that the recrystallization is difficult to be promoted during the post-processing treatments. Generally, the static recrystallization temperature of the nickel-base superalloy is in the range of 1000-1100 °C [69], and recrystallization will gradually take place under this temperature range.

However, according to extensive investigations, the super- γ' -solvus treatment is the only essential way to achieve recrystallization. For example, Kunze et al. [70] reported that the as-laser deposited IN738LC superalloy even retains the strong cubic texture although it went through a super-solvus HIP at 1180 °C for 4 h. Similarly, in the previous study on LPBF IN738LC superalloy [71], a combination of thermal treatments including 1210 °C HIP for 4 h plus 2-h solutioning at 1120 °C and 24-h aging at 850 °C failed to bring a fully recrystallized microstructure. Moreover, to eliminate the crystallographic texture induced by LPBF in IN738LC, Geiger et al. [72] applied a full heat treatment including a super-solvus heat treatment at 1250 °C for 3 h followed by a 1200 °C HIP for 4 h, 1120 °C solution treatment for 2 h, and a 20 h aging at 850 °C. In the report by Messé et al. [73], the recrystallization of LPBF IN738LC occurs at around 60 °C above the γ' solvus with a narrow temperature window of recovery to recrystallization transition of approximately 10 °C. Conversely, in the conventionally processed γ' -strengthened nickel-base superalloy, Dahlén et al. [74] reported that at a sub- γ' -solvus temperature of 1120 °C (45 °C below the γ' solvus (~ 1165 °C)), the cold deformed IN738LC gradually recrystallized, where approximately 80% recrystallization and full recrystallization were achieved after 2 h and 4 h, respectively.

Consistent observations were found in another commonly printed non-weldable γ' strengthened nickel-base superalloy CM247LC, that exhibits a narrow gap of recovery to the recrystallization transition temperature. According to Muñoz-Moreno et al. [75], the as-built CM247LC superalloy keeps the strong (001) fiber texture after 2-hour heat treatment at 1230 °C, however, after treatment at 10 °C higher (1240 °C for 2 h) the recrystallization occurred extensively and reduced the crystallographic anisotropy, at a mesoscale across the investigated sample.

The recrystallized grain structure is highly demanded by the high-temperature application, thanks to the coarse and more equiaxed recrystallized grains. However, the recrystallization induced loss of tensile ductility was reported by Ghoussoub et al. [76]. Similar lack of tensile and creep ductility of super-solvus treated specimens can be found in

this study. It is worthy to re-thinking if the recrystallized grains in LPBF superalloy benefit the high-temperature mechanical properties.

2.4.2 Post-process treatment-induced cracking

Besides the in-process cracking, two more types of cracking, i.e., strain-age cracking and ductility-dip cracking, are introduced during the post-processing treatment.

2.4.2.1 Strain-age cracking

During the post-processing treatment, at particular the aging temperatures, the formation of precipitates reduces the ductility of this material. The precipitation of the intermetallic γ' phase on one hand increases the strength of nickel-based superalloys, while on the other hand, decreases their ductility. As a consequence, the un-released RS plus the precipitation stress could induce strain-age cracking (SAC) when the strain exceeds the ductility limit [77]. The SAC generally leads to the crack in macro-scale in the length dimension of millimeter. Owing to the high SAC susceptibility of γ' -strengthened nickel-based superalloys, the post-processing treatment remains a big challenge.

2.4.2.2 Ductility-dip cracking

In the γ' -strengthened nickel-based superalloys, the ductility dip was generally found as the high reduction of ductility in the critical intermediate temperature range such as 700 to 900 °C as reported by Kim et al. [78]. For example, as reported for a Monel K-500 superalloy, the ductility is largely reduced from higher than 20% elongation at 300 °C to around 2% elongation at 650 °C [79]. The ductility-dip cracking (DDC) can be generated during the post-AM processing, and present intergranular cracking features [80]. Similar to the SAC, DDC would occur once the material is undergoing this low-ductility region with high enough strain applied [81].

2.5 History and development of nickel-based superalloys

2.5.1 Development of alloy composition

The terminology 'superalloy' was firstly introduced in the 1950s, for describing alloys with both good high-temperature mechanical and chemical properties [82]. This meaning of 'superalloy' seems to be rather obscure, compared with the other nomenclatures, like 'heat-resisting alloys' or 'high-temperature alloys'. In Tien and Caulfield's textbook [83], they credit the popularity of the term 'superalloy' to the popular fictional figure Superman, who influenced the use of the word 'super' as a descriptor. At the earlier stage before the superalloy being named as 'superalloy', the superalloy-like high-temperature metallic materials were already adapted for high-temperature components. For example, in 1905, Marsh [84,85] developed the Nichrome alloy, which comprises of 80% of nickel and 20% of

chromium as the material for turbine blades application. In 1921, a patent including the HASTELLOY® B nickel-molybdenum alloy was filed, and it was still used in the space capsule and the Atlas rocket in 1961 [86]. In the 1930s, a British austenitic iron-based Cr-Ni-W alloys alloy, KE965, was selected as the 'standard' alloy for exhaust valves in both the aircraft and automobile industries [87]. For both the early-stage superalloys like HASTELLOY® B and KE965 superalloys, they are basically austenitic base alloys. To further improve the mechanical properties at elevated temperatures, Pfeil [88] developed the Nimonic 80 superalloy in 1941, by adding small amount of alloying elements, such as aluminum and titanium, in the Nichrome base alloy. Since then, Nimonic 80 is 'literally' the first γ' phase ($\text{Ni}_3(\text{Al}, \text{Ti})$) strengthened nickel-based superalloy. The development of the Nimonic 80 superalloy laid the foundation for the concept of γ' as the principal strengthening source at elevated temperatures for superalloys, even though meanwhile various alloying elements have been doped for different purposes. In 1958, Eiselstein [89] firstly introduced Ni_3Nb γ'' as the strengthening phase and developed the well-known Inconel 718 superalloy. Till now, Inconel 718 and its derivatives are still active in the center of superalloy's arena acting as the one of most widely used superalloy. With more and more diverted nickel-based superalloys being proposed through the past several decades, the high-temperature components are offered by better and better performing materials.

However, the understanding of nickel-based superalloys is more serendipitous. The development of early generations of superalloys has largely relied on metallurgical experience and expertise, hypothesis, and even sometimes accidental luck. As mentioned above, Pfeil developed the first γ' -strengthened superalloy Nimonic 80 in 1941, while the γ' phase was firstly recognized by Taylor and Floyd by their working on Ni-Ti-Al ternary system a decade later in 1952 [90]. In addition, the first direct observation of γ' precipitates in a superalloy was conducted by Betteridge and Franklin using micrography in 1957 [91]. Hereafter, with the rapid development of phase diagram theory, physical metallurgy, and advanced microstructural characterization, the nickel-based superalloy developments are more and more relied on tailoring microstructure by composition modification using these powerful scientific tools. The development of the RR1000 superalloy for turbine disc applications is one of the most successful cases. Hardy et al. [92] in Rolls-Royce plc., proposed the RR1000 superalloy with a good combination of damage tolerance and creep resistance based on the thermodynamic modeling from phase diagram analytics, which abandons the traditional iteration involved empirical alloy design method. In recent years, with the assistance of high-throughput computational thermodynamics coupled with physics-based approaches, e.g. under the protocol of Alloy-by-Design® (ABD) [93], γ' -strengthened cracking-resistant ABD-850AM and ABD-900AM nickel-based superalloys were developed for the AM process [94].

2.5.2 Development of manufacturing processes

The better performances of nickel-based superalloys are impossible to be achieved solely by the chemical composition development, while the development of manufacturing

processes also play an important role. Together with the flourishing development of chemical composition since the 1950s, the manufacturing processes experienced the corresponding rapid development as well. The first milestone worth mentioning is the introduction of glass lubrication for extrusion process by Sejournet in 1948 [95], enabling a larger ingot to be extruded to bars for machining, or to billets for the following thermomechanical processing steps.

Besides the wrought-related manufacturing processes which were extensively used for superalloy production, with the development of casting techniques, turbine blades with complicated internal cooling system were commonly fabricated by precision castings. In 1952, Darmara [96] firstly developed the commercial vacuum melting technique, which significantly improved the cleanliness and provided more accurate composition control compared with the air melting. With vacuum melting, the ambient environmental contamination, e.g., nitrogen and oxygen pickup from the atmosphere, was dramatically reduced. In addition, a larger number of alloying elements, especially the refractory elements, are possible to be added via vacuum melting process. Then, the casting superalloys started to overtake the wrought ones for the turbine blade application. Although the wrought superalloys show lower elemental segregation and better mechanical and cyclic properties at the relatively lower operating temperature, the casting parts are superior on the high-temperature performance partly owing to the much coarser grain size. Until date, vacuum melting has been the primary method of producing nickel-based superalloy ingots. In the late 1960s, Versnyder et al. [97] further developed a new precision investment casting technique, thus the directional solidification (DS). Directional solidification is based on the Bridgman–Stockbarger method by controlling the direction of the temperature gradient during solidification. By applying the grain selector or the monocrystal ‘seeding’ on controlling the early-stage directional solidification process, the nickel-based superalloy can then be produced with columnar grain or single crystal form. Consequently, the transverse grain boundaries (to the loading direction) have been highly eliminated, ensuring a dramatic improvement of the creep resistance at elevated temperatures.

Another widely used manufacturing route for nickel-based superalloy is the powder metallurgy approach. Powder metallurgy processing was developed as a near-net-shaping manufacturing technique with low-mass waste to fabricate nickel-based superalloy parts in the late 1960s. Generally, the powder metallurgy approach contains a route of powder production, powder consolidation, and thermomechanical processing [98]. Thanks to the use of pre-alloyed powders, the elemental segregation is restricted in the powder-size dimension. In addition, equiaxed fine grains are commonly developed in the powder metallurgy processed superalloys. According to these microstructural advantages of the powder metallurgy superalloys, the fatigue crack propagation resistance, which is one of the major critical requirements for the turbine disc component, is excellent.

2.6 Physical metallurgy of nickel-based superalloy

The physical metallurgy of nickel-based superalloy is discussed in this section. It includes the chemical composition (alloying elements), microstructure (phases), property (mechanical and chemical properties) about nickel-based superalloys.

2.6.1 Phases and microstructures

Typically, a certain superalloy contains different phases. In a modern γ' -strengthened superalloy, the common phase configuration consists of disordered austenite FCC phase named as γ phase, and ordered FCC phase with $L1_2$ crystal structure named as γ' phase. The γ phase is mostly composed of Ni atoms, with other alloying element atoms randomly substituting other FCC lattice sites. In the γ' phase, Ni atoms occupy the face centers, while alloying elements Al, Ti, or Ta are substituting the vertices of FCC cubic cells. In some other precipitation-strengthened nickel-based superalloys, such as IN718, IN625, and Rene220, the more common precipitate phase is γ'' (gamma double prime). The γ'' phase is body-centered tetragonal (BCT) with the $D0_{22}$ crystal structure, in which the chemical composition formula is Ni_3Nb . It should be mentioned that γ'' phase is a thermodynamically metastable phase. At the elevated temperature above 650 °C, it decays to its thermodynamically stable form (the δ phase with $D0_a$ crystal structure, sharing the same chemical composition of Ni_3Nb) [99]. To this extend, it precludes the application of γ'' -strengthened superalloy at an operating temperature higher than 650 °C.

Besides the major phases as γ matrix and the γ' precipitates, there are other phases in smaller amounts but still play influential roles. Firstly, the carbides. Two types of carbides are commonly recognized in superalloys, thus the primary and secondary carbides. For primary carbide, it is formed during the solidification process and act as the carbon reservoir for other carbides which can be developed during the following heat treatment and/or service conditions. The primary carbide is in the form of MC, where M stands for metallic element. The distribution of MC carbides is usually found throughout the alloy at both grain bulk and grain boundaries. However, it may not be the case for AM processed superalloys, in which the carbides are normally located at the grain and subgrain boundaries. Commonly observed MC carbides are HfC, TaC, NbC, and TiC, according to their low Gibbs free energy of formation and the experimental observations [100].

At elevated temperatures, MC carbides decompose to secondary carbides. For example, the M_6C and $M_{23}C_6$ type carbides. The M_6C carbides form at 815-980 °C, while the $M_{23}C_6$ carbides form at a slightly lower temperature of 760-980 °C [101]. Different from the MC carbides, secondary carbides prefer to reside in the intergranular interfaces. Therefore, the secondary carbides are beneficial to hinder the grain boundary sliding, generally leading to an improved high-temperature mechanical property. In addition, this advantage has been also taken to control the grain size during the thermomechanical processing, also owing to the pinning against grain boundary migration. Compositionally, secondary carbides are enriched with Cr, Mo, and W.

Secondly, the borides. Boron is another commonly doped minor element and known as grain boundary 'strengtheners'. In nickel-based superalloys, boron is prone to segregate at the grain boundary regions. The intergranular borides can significantly toughen superalloy at high temperature via improved ductility. The common form of boride is $M_2M'B_2$, where M represents the boride forming elements with larger atomic radius like Mo and Ti, and M' represents those smaller elements like Cr, Ni, and Co [102].

Thirdly, the topologically close-packed (TCP) phases. The TCP phases in superalloys can form during the heat treatment or long-term operation. The morphology of these phases is often plate-like or needle-like. The existence of the TCP phases, such as σ , μ , and P phase, is detrimental to the phase stability of superalloys. The excessive quantities of heavy elements, such as Cr, Mo, W, and Re (a common alloying element doped in single crystal superalloy) are prone to develop TCP phases. For example, the ideal stoichiometry of the σ phase is A_2B , where A and B stand for the transition metals, like $Cr_{61}Co_{39}$, $Re_{67}Mo_{33}$; of μ phase is A_6B_7 , like W_6Co_7 , and Mo_6Co_7 ; one of the compositions for P phase is $Cr_{18}Mo_{42}Ni_{40}$ [103].

2.6.2 Alloying elements effects

Up to ten or more alloying elements are intentionally added to a modern nickel-based superalloy. The selection of elemental additions is generally motivated by the desire to improve properties at high temperatures. The typical alloying elements in nickel-based superalloys and their features are summarized as follows [104,105] in Table 2.1:

Table 2.1. Alloying elements and their roles in nickel-based superalloys.

Element	Atomic number, Z	Atomic radius (pm)	Roles in nickel-based superalloys
Ni	28	149	Matrix material; solvent.
Cr	24	166	Hot corrosion and oxidation resistance; solid solution strengthener; σ phase former; secondary carbide former.
Co	27	152	High solubility in Ni matrix; increasing γ phase solidus; precipitates modifier.
Mo	42	190	Strong solid solution strengthener; boride former; MC and M ₆ C carbide former; σ and μ phase promoter.
W	74	193	Strong solid solution strengthener; M ₆ C carbide former; σ and μ phase promoter.
Al	13	118	Primary γ' former; improve high-temperature oxidation resistance by forming alumina.
Ti	22	176	γ' former; strong MC carbide former.
Ta	73	200	MC carbide former; increasing γ' phase fraction; strong solid solution strengthener.
Nb	41	198	Strong solid solution strengthener; increasing γ' phase fraction; MC carbide former; typical γ'' former.
Re	75	188	Solid solution strengthener; precipitates modifier.
Ru	44	178	Solid solution strengthener; phase stabilizer in Re containing superalloys.
C	6	67	Carbide source; solid solution strengthener.
B	5	87	Boride source; grain boundary strengthener; increasing creep strength and ductility.
Hf	72	208	Strong MC carbide former; grain boundary strengthener.
Zr	40	206	Grain boundary strengthener.

2.6.3 Strengthening mechanisms

Several distinct mechanisms contribute to strengthening of nickel-based superalloys.

2.6.3.1 Solid solution strengthening

The solid solution strengthening is attributed to the local stress field caused by the solid solutes in the base metal matrix. This stress field is effective on impeding the dislocation movements. In nickel-based system, as mentioned above, owing to up to more than 10 different alloying elements, the contribution of solid solution strengthening on the strength is significant. To mathematically quantify the solid solution strengthening, a compositional average based approach is generally used, where the strengthening coefficients of solid solutioning from each alloying elements are obtained from experimental results and described in detail by Roth et al. [106].

2.6.3.2 Precipitation strengthening

In superalloys, the γ' phase is the primary precipitation strengthener, especially in terms of high-temperature strength. The $L1_2 \gamma'$ compound shows an anomalous temperature-dependent yield strength effect [107]. At higher temperatures, e.g. at 900 °C the γ' materials display the peak yield strength, which is double the strength at room temperature [103,108].

On the other hand, the γ' precipitates within the γ matrix play various roles in the dislocation/precipitate interaction. First, the γ' phase can be sheared by gliding dislocations. Owing to the ordered structure of γ' phase, a large energy penalty would be generated if one full dislocation ($a/2 < 1\bar{1}0 > \{111\}$) moves through the γ' phase. This energy is known as the anti-phase boundary (APB) energy. The origin of APB is caused by the low-energy Al-Ni bond being forced to be replaced by the unfavorable Al-Al bond. Therefore, dislocations commonly go through the γ' in a pair instead, where the APB generated by the first dislocation will be erased by the second dislocation in this fashion. For dislocation shearing, it can be further categorized into weakly coupled and strongly coupled dislocation manners [109]. In the weakly coupled dislocation case, the separated distance between the dislocation pair is greater than the diameter of γ' phase, while in contrast the strongly coupled dislocation case indicates that this distance between the paired dislocations is smaller than the diameter of γ' phase, thus, the leading and trailing dislocations could be somewhat observed at the same particle [110]. Second, if the size of precipitate exceeds a critical value, dislocation bypassing by Orowan looping [111] is more operative than dislocation shearing, owing to the stress required for bypassing (τ_{Oro}) can be lower than the stress required for cutting (τ_{cut}).

Here, for a given γ' precipitate, e.g. 300 nm in diameter, one could give the estimated τ_{cut} by strong pair coupling as: $\tau_{cut} = Gb/(\pi L_{\gamma'-\gamma'})\sqrt{(\pi d_{\gamma'}\gamma_{APB}/(Gb^2) - 1)}$ [112]. While the shear stress for Orowan looping is written as: $\tau_{Oro} = Gb/L_{\gamma'-\gamma'}$, where G is the shear modulus (taken as 75 GPa), b is the magnitude of Burger's vector (0.257 nm), $L_{\gamma'-\gamma'}$ is the spacing between particles (taken as 112 nm as the case in the appended paper I), $d_{\gamma'}$ is the average size of

precipitate (300 nm), γ_{APB} is the anti-phase boundary energy (0.2-0.3 J/m²). After calculation, it results in $\tau_{cut} > 333$ MPa, however, τ_{oro} is approximately 170 MPa. It implies that dislocation bypassing is more common in the coarse γ' precipitates condition.

2.6.3.3 Grain boundary strengthening

The idea that the grain boundary network strengthens polycrystalline alloys is a classic topic. The GBs impede the dislocation gliding which strengthen the materials. To a certain range of grain size, the yield strength increases with decreasing the grain size. And the most famous relationship between the increment of yield strength and the grain size is the Hall-Petch equation [113,114].

2.6.3.4 Dislocation strengthening

In crystals, dislocation is a common line defect. Considering a small volume swept by edge dislocation, the shear strain can be expressed as [115]:

$$d\gamma = \rho bl \quad (2.2)$$

Here the $d\gamma$ is the unit shear strain, ρ is the dislocation density, b is the magnitude of Burger's vector, and l is the length of the given dislocation line. Assuming a uniform distribution of dislocations, the length of dislocation line l is given by the reciprocal of the square root of dislocation density as:

$$l = \frac{1}{\sqrt{\rho}} \quad (2.3)$$

The strengthening contribution from dislocations is expressed by introducing the shear modulus G to the shear strain as:

$$\Delta\sigma = \alpha_{\tau_{ay}} \cdot M G b \sqrt{\rho} \quad (2.4)$$

Where $\alpha_{\tau_{ay}}$ is a constant and M is Taylor's factor and this equation is well-known as Taylor's equation [116]. According to Taylor's equation, the corresponding increase of strength is proportional to the square root of dislocation density. In the LPBF alloys, especially in the as-built condition where high density of dislocation is generally obtained, the strengthening contribution from dislocations is significant. For example, the as-built LPBF IN738LC superalloy shows excellent yield strength at ambient temperature even though it lacks the γ' precipitates. The reference [18] gives a detailed discussion on the strengthening and embrittlement mechanisms.

2.7 Creep in nickel-based superalloys

Creep of materials is a time-dependent deformation process of solid materials at elevated temperature, which is normally higher than 50% of its melting temperature.

2.7.1 Creep mechanisms

According to the classical Ashby deformation mechanism map [117], the creep deformation could be categorized into diffusional creep and dislocation creep. In the diffusional creep regime, the creep deformation rate is determined by the diffusional flow rate. Considering that the grain boundaries in polycrystalline materials act as the major sources and reservoirs for vacancies and atoms, then the diffusional creep could be further subdivided into Nabarro-Herring [118,119] and Coble [120] creep. The difference is from the diffusion path, wherein Nabarro-Herring creep, the lattice diffusion is only considered, while in Coble creep, the grain boundary diffusion is the consideration.

For precipitation-strengthened alloys, such as the γ' -strengthened nickel-based superalloys, the dislocation creep is operative at relatively lower temperature and higher stress, compared with the diffusional creep conditions. The dislocation travels along the slip plane until it encounters a precipitate obstacle, then dislocation climbing can occur with the assistance of thermal activation [121]. For example, in the regime of dislocation climb controlled creep, Reed [122] denote M_{creep} as a suitable merit index for creep resistance of single crystal superalloys:

$$M_{creep} = \sum_i \frac{x_i}{\bar{D}_i} \quad (2.5)$$

Where x_i is the atomic fraction of solute i in the alloy, and \bar{D}_i is the appropriate interdiffusion coefficient. It is worth noting that having more slow diffusing atoms results in superior creep rate resistance and lower dislocation climbing rate, according to the expression. On other hand, for the creep of the polycrystalline nickel-based superalloys, the grain boundary sliding acts as the creep rate controlling part, which is discussed in detail in the appended paper I.

2.7.2 Creep performance of LPBF processed superalloys

Larson and Miller [123] proposed a method to estimate the time-temperature relationship under creep stress, and it is the most widely used parameter. Larson Miller Parameter (LMP) can be described as the following:

$$LMP = T \times (c_{LM} + \log_{10} t) \quad (2.6)$$

Where T is the absolute temperature in Kelvin; c_{LM} is the Larson-Miller constant, which varies between 15 and 25, and is taken to be 20 in this study; t is the time to rupture. According to this expression, LMP is directly related to creep temperature, but rupture time has a less logarithmic dependence. It also should be noted here, using constant c_{LM} the value

may result in the overestimation of the creep strength at long-term service, especially for the materials sensitive to microstructural degradation [124].

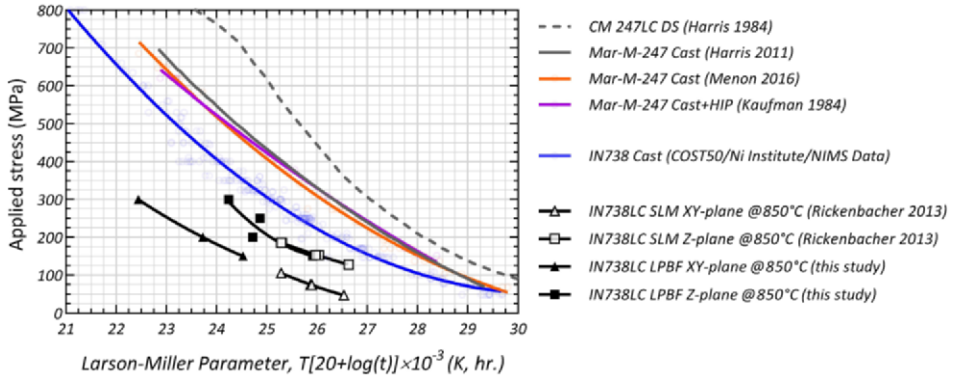


Fig. 2.2. Larson-Miller-Parameter creep comparisons of CM247LC, Mar-M-247, IN738 nickel-based superalloy by casting, as well as LPBF fabricated IN738LC (data from references [32,70,125–130] and this study).

The creep performance of legacy superalloys CM247LC, Mar-M-247, IN738, and LPBF IN738LC are compared in the LMP plots in Fig. 2.2. Here, CM is a trademark of Cannon-Muskegon Corporation, Mar-M is a trademark of Martin Marietta Corporation, and IN(Inconel) is a trademark of Special Metals Corporation. The CM247LC DS shows the most superior creep properties among the demonstrated alloys thanks to the highly reduced transverse grain boundaries. Then, cast Mar-M247 superalloy shows better creep resistance properties than cast IN738, which can be attributed to the higher γ' precipitates volume fraction in Mar-M247. In addition, Mar-M247 superalloy is alloyed with more refractory elements Mo, W, Ta, and Hf with an additive sum of more than 15 wt. %, compared to a summation of <10 wt. % in IN738. Due to their slowly diffusing natures, these refractory elements can improve the creep performance of superalloys. From the early study of LPBF IN738LC, Rickenbacher et al. [32] reported the creep performance at 850 °C. The specimens were subjected to HIP cycle and standard heat treatment. The bars are examined from vertically (Z-plane) and horizontally (XY-plane) building direction. In this study, the similar LPBF IN738LC superalloys were also examined under creep at 850 °C from both building directions. More creep results are presented in section 6.5 Creep property of LPBF superalloys. The creep results of LPBF IN738LC superalloys are highly consistent as plotted in the LMP diagram. However, the creep property of LPBF IN738LC is inferior to the cast ones.

2.8 Chapter summary

The background of the LPBF process and nickel-based superalloy is reviewed in this chapter. It is a frank conclusion that nickel-based superalloy is one of the most important and well-developed alloy systems. Meanwhile, in the last 2-3 decades, AM techniques have been growing rapidly, operating as a disruptive manufacturing process in comparison to conventional ones. The microstructure of AM fabricated parts deviates significantly from well-known knowledge in many ways, particularly in terms of cellular structure, chemical distribution, and phase configuration. This facilitated and encouraged the development of novel superalloys composition adapted to the AM process. Despite the fact that there have been few successful cases documented on this topic and that there appears to be a significant knowledge gap, attempts at chemical modification should be encouraged.

Chapter 3 Experimental methodology

3.1 Materials

Multiple γ' -strengthened nickel-based superalloys are used in this study, including MAD542 [131], alloy738+, the legacy superalloy IN738LC and its derivatives [18,71,132], and CM247LC [133]. MAD542 is a newly designed γ' -strengthened superalloy for the LPBF process. Alloy738+ is a chemistry modified alloy from IN738 superalloy composition, with improved crack resistance during the LPBF process. IN738 is a cast nickel-based superalloy first developed by Bieber et al. [134] from the International Nickel Company, Inc. in the 1960s. CM247LC is a chemistry modified superalloy from the parent alloy Mar-M247, by Harris et al. [125] from the Cannon-Muskegon Corporation in the 1970s. The chemical compositions of the pre-alloyed powder are listed in Table 3.1.

Table 3.1. Chemical composition of LPBF superalloys used in this study (Ni in Bal.).

Alloy		Cr	Co	Mo	W	Al	Ti	Ta	Nb	C	B	Zr	Hf
IN738LC-LB/LZr	wt.%	15.9	9.2	1.72	2.8	3.2	3.3	1.72	0.9	0.102	0.007	0.005	/
	at.%	17.4	9.0	1.02	0.9	6.8	3.9	0.54	0.6	0.484	0.037	0.003	/
IN738LC-HB/LZr	wt.%	16.2	9.3	1.76	2.8	3.3	3.4	1.7	0.9	0.107	0.03	0.006	/
	at.%	17.7	9.0	1.04	0.9	7.0	4.0	0.53	0.6	0.506	0.158	0.004	/
IN738LC-LB/HZr	wt.%	16.0	9.2	1.75	2.8	3.2	3.4	1.72	0.9	0.11	0.002	0.04	/
	at.%	17.5	9.0	1.04	0.9	6.8	4.0	0.54	0.6	0.522	0.011	0.025	/
IN738LC-HB/HZr	wt.%	16.0	9.3	1.72	2.9	3.2	3.3	1.73	0.9	0.11	0.03	0.07	/
	at.%	17.5	9.1	1.02	0.9	6.8	3.9	0.54	0.6	0.522	0.158	0.044	/
IN738LC-1	wt.%	16.0	9.3	1.72	2.9	3.2	3.3	1.73	0.90	0.11	0.03	0.07	/
	at.%	17.5	9.1	1.02	0.9	6.8	3.9	0.54	0.55	0.52	0.16	0.04	/
IN738LC-2	wt.%	15.9	8.5	1.69	2.6	3.6	3.4	1.72	0.92	0.12	<0.001	<0.001	/
	at.%	17.4	8.3	1.00	0.8	7.5	4.0	0.54	0.56	0.57	<0.01	<0.002	/
IN738LC-7	wt.%	15.7	8.3	1.80	2.6	3.4	3.3	1.80	0.90	0.11	0.01	/	/
	at.%	17.2	8.1	1.07	0.8	7.2	3.9	0.57	0.55	0.52	0.05	/	/
IN738LC-E	wt.%	17.2	9.4	1.90	2.6	3.5	3.6	1.74	0.90	0.10	0.02	0.03	/
	at.%	18.7	9.1	1.12	0.8	7.4	4.3	0.54	0.55	0.48	0.10	0.02	/
IN738LC-M	wt.%	16.2	8.5	1.80	2.4	3.5	3.5	1.70	1.00	0.10	0.01	/	/
	at.%	17.7	8.2	1.06	0.7	7.4	4.1	0.53	0.61	0.47	0.05	/	/
Alloy738+	wt.%	14.0	8.6	1.77	2.7	4.7	1.5	2.0	1.6	0.10	<0.001	<0.002	/
	at.%	15.3	8.3	1.04	0.8	9.9	1.8	0.63	0.98	0.47	<0.01	<0.002	/
MAD542	wt.%	8.0	8.0	5.0	4.0	5.0	1.0	3.0	2.0	0.1	<0.001	<0.002	/
	at.%	9.0	8.0	3.1	1.3	10.9	1.2	0.97	1.26	0.49	<0.01	<0.002	/
CM247LC	wt.%	8.5	8.7	0.60	9.2	5.5	0.7	3.50	/	0.07	0.01	0.01	1.24
	at.%	9.8	8.9	0.37	3.0	12.2	0.9	1.15	/	0.35	0.07	0.01	0.41

3.2 LPBF process

To fabricate the abovementioned LPBF superalloys with a minimum defect level, optimized LPBF parameters were usually used. For example, to explore the LPBF processing window of IN738LC-LB/LZr, IN738LC-HB/LZr, IN738LC-LB/HZr, IN738LC-HB/HZr, Alloy738+, and MAD542 superalloy, the identical Design of Experiment (DoE) matrix has been used. The detailed processing parameters have been presented in Table 3.2. Optimized printing parameters have been used for LPBF CM247LC as documented in [135] in detail. In general, to fabricate the samples for microstructural-based study, an EOS M100 LPBF system equipped with a 100 mm round base plate was used. For printing most of the mechanical testing samples, EOS M290 with $250 \times 250 \text{ mm}^2$ square build plate is more commonly used. All the prints were conducted under the argon flow protection.

Two building directions (BD) were used for fabricating the parts as horizontally built (HB) and vertically built (VB). Here, the BD of the HB sample is perpendicular to the longitudinal direction of the sample, thus in most cases, perpendicular to the loading direction during mechanical testing. In contrast, the BD of VB samples is parallel to the longitudinal direction, thus parallel to the loading direction.

Table 3.2. DoE parameters used in this study (layer thickness: $20 \mu\text{m}$).

Exp.	Laser power, P (W)	Scan speed, V (mm/s)	Hatching distance, H (μm)	Energy density, E (J/mm^3)
#1	100	1000	50	100
#2	170	1000	50	170
#3	100	1300	50	77
#4	170	1300	50	131
#5	100	1000	70	71
#6	170	1000	70	121
#7	100	1300	70	55
#8	170	1300	70	93
#9	135	1150	60	98

3.3 Metallographic preparation

For metallographic sample preparation for a number of diverse microstructural characterization methods, such as optical microscopy and scanning electron microscopy, the traditional mounting-grinding-polishing routine was used. To begin the hot mounting process, PolyFast, a carbon-based thermosetting glue, was utilized to prepare the Ø30 mm mount. The mount is then ground using #220 SiC sandpaper with water as a lubricant. The polishing was done in three steps: first with a 9 µm abrasive, then with a 3 µm abrasive, and finally with Struers® OP-U colloidal silica suspension.

3.4 Optical microscopy

In this study, light optical micrograph imaging on the well-polished metallographic sample was commonly used for detecting the as-built defects. A Leica DM6 optical microscopy (Leica Microsystems GmbH, Wetzlar, Germany) was used for this purpose. To inspect the fracture surface, a Leica M205C stereo optical microscopy was used. Both of the optical microscopies were equipped with the Z-stack function.

3.5 Electron microscopy

3.5.1 Scanning electron microscopy

The SEM characterization was performed with a Hitachi SU70 field emission scanning electron microscope (FE-SEM) (Hitachi, Ltd., Japan) equipped with energy dispersive X-ray spectroscopy (EDS) and wavelength dispersive X-ray spectroscopy (WDS) detectors. For imaging secondary electron (SE) and backscattered electron (BSE) micrographs, a 20 kV acceleration voltage was commonly utilized.

3.5.2 Electron backscatter diffraction

Electron backscatter diffraction (EBSD) is a crystallographic orientation-based characterization method under SEM. The Kikuchi diffraction patterns were detected using an Oxford NORDLYS EBSD detector (Oxford Instruments, UK). In most cases, a 20 kV acceleration voltage was used. The Flamenco software was used to collect and index the EBSD data (Oxford Instruments HKL CHANNEL 5). An open-source MATLAB® tool-box MTEX (version 5.3) [136], was used for the post-analysis of the EBSD scan.

3.5.3 Transmission electron microscopy

Transmission electron microscopy (TEM) analysis was conducted on an FEI Tecnai G2 microscopy, operating at 200 kV accelerating voltage. To prepare the TEM sample, first, a thin foil was ground down to 50-100 µm in thickness using abrasive paper with water as the

lubricant. Then a round foil with a diameter of 3 mm was punched. The final step of electropolishing was performed using a Struers twin-jet apparatus. The electrolyte solution was 10% perchloric acid and 90% ethanol. The polishing temperature was -25°C , and the polishing voltage was 20 V.

3.6 Etching

To image the morphology of γ' precipitates under SEM, etching was usually applied. There are two types of etching methods used in this study: chemical etching and electro-etching.

3.6.1 Chemical etching

For chemical etching, the well-polished metallographic samples were immersed in Marble's reagent at the ambient temperature, until the surface turns from a bright mirror-like finish to greyish color. The time for immersion depends on the γ' volume fraction of the sample, for a superalloy with 60% of γ' , 5–15 s is suggested. After chemical etching, the sample surface was first cleaned in water. Then it was ultrasonic cleaned under ethanol. This etching reagent dissolves the γ' phase.

3.6.2 Electro-etching

Well-polished samples were connected to the anode while a nickel plate was used as the cathode. The sample and cathode were immersed in the electrolyte of 10% phosphoric acid solution. The applied direct voltage and etching time are determined by the surface area and the γ' fraction. For a superalloy with 60% of γ' , a voltage of 10 V was selected, and the electro-etching time lasted for approximately 5 s. This etching dissolves the γ matrix while γ' precipitates remain.

3.7 Mechanical testing

3.7.1 Tensile testing at room temperature

Room-temperature tensile testing was performed on an Instron 5582 universe testing system with a nominal strain rate of 10^{-3} /s. A dog-bone-shaped solid specimen was used with a gauge length of 25 mm and a gauge diameter of 5 mm. An extensometer with two knife edges attached to the gauge length surface was used for the engineering strain measurement. The gauge length of the extensometer was 12.5 mm.

3.7.2 Slow strain rate tensile testing

SSRT tests were performed on an Instron 5982 testing system with a 100 kN load capacity, in lab air. A three-zone Instron SF-16 resistance furnace was used for providing a high-temperature atmosphere. A type-K thermocouple was attached to the middle position of the testing bar to control and monitor specimen temperature. A 2-h soak time was waited at the target temperatures before starting the mechanical testing. Load control with +/- (tension/compression) 10 N range was used to protect the testing bar from early-stage deforming caused by thermal expansion during heating and soaking. To measure the engineering strain, an Instron 7361C high-temperature extensometer with a ceramic rod was used. The gauge length of the extensometer is 12.5 mm. The V-shape ceramic tips of the extensometer were directly attached to the surface of the testing specimen at the gauge section. A damper was used to reduce the noise from ambient vibrating. For example, for the gauge length of 24.5 mm, various constant displacement rates were used for SSRT tests at 0.147, 0.0147, 0.00147, and 0.000147 mm/min, which are equivalent to the nominal strain rates of 10^{-4} , 10^{-5} , 10^{-6} , and 10^{-7} s⁻¹. Before applying the slow displacement rate control, to fully engage the connection between test bar/fixtures, all the specimens were pre-loaded to approximately 25 MPa engineering stress (500 N for gauge diameter=5 mm; 320 N for gauge diameter=4 mm) by the tension of strain rate of 10^{-3} s⁻¹.

High-temperature tensile testing has been performed in the same testing rig and setup. For high-temperature tensile loading, the nominal strain rate of 10^{-3} s⁻¹ was commonly used.

3.7.3 Creep testing

Creep tests were performed on a ZwickRoell KAPPA 050 DS electromechanical creep testing system based on the ISO 204 international standard [137]. The creep testing was performed in lab air. A ZwickRoell universal 3-zone furnace was used. Three type-N thermocouples were attached to the gauge section of the testing bar to monitor the specimen temperature. After reaching the target temperature and a waiting time of 4 h, the test started. A rod and tube extensometer was used to clamp the 'shoulders' of the testing bar. The strain was read from the displacement meter outside of the furnace. The creep specimen was pre-loaded at approximately 25 MPa engineering stress in tension before heating and soaking.

3.8 Oxidation testing

Oxidation tests were conducted on cylinder samples with a diameter of 8 mm and a length of 10 mm. Before the test the samples were polished with 1200 grit sandpaper, leading to a surface roughness of $R_a=0.095$ μm and $R_z=1.142$ μm . Then the specimens were ultrasonic cleaned in acetone for 15 min to remove the surface contaminations.

Two types of oxidation tests were conducted in lab air: isothermal and cyclic oxidation. For isothermal oxidation testing, the oxidation specimens were held in a Haldenwanger™ tall melting crucible with a height of 34 mm to collect the spalled oxides. Mass changes were

weighted together with crucibles. For cyclic oxidation testing, the oxidation specimens were placed on ceramic boats. For each cycle, the samples were air-cooled from the oxidation to room temperature and the oxide spallation was gently removed by a soft brush before weighting.

Nabertherm Muffle furnaces were used for the oxidation test. The oxidation temperatures are 850 °C, 950 °C, and 1050 °C. The temperature was monitored by independent type-K thermocouples externally. Before tests, the crucibles were baked at 50 °C higher than the oxidation temperatures. A Mettler Toledo® AG245 analytical balance was used for weighting which has the 10^{-5} g resolution.

Chapter 4 Crack susceptibility model

As documented in the previous chapters, high-strength nickel-based superalloys normally show high crack-susceptibility during the LPBF process. It's a similar but not the same phenomenon observed in the welding cracking of this kind of superalloys. For decades, the weldability of precipitation-hardened nickel-based superalloys was qualitatively predicted in Prager and Shira's book [138] from 1968. In their model, the superalloys are categorized into different regions according to their high SAC tendency. The contents of γ' formation element, in particular, Al and Ti of the superalloy grades were plotted, and an $\text{Al (wt.\%)} + 0.5 \times \text{Ti (wt.\%)} = 3 \text{ (wt.\%)}$ boundary was most commonly used, where the alloy has more Al and Ti would likely show larger risk on SAC, and vice versa. In a recently developed LPBF superalloy, a modified weldability diagram is utilized for accessing the SAC tendency [139].

Other crack susceptibility models are aiming at estimating an alloy's freezing range, based on the understanding that shrinking the mushy zone during solidification reduces crack susceptibility. Thus, the sensitivity of the hot tearing of an alloy increases with the broadening of the freezing range [140]. This type of criterion has been frequently documented in casting or welding research. The very common form to express this interval of solidification is by calculating the temperature interval [141] between the point at which the liquid feeding becomes difficult ($\sim 90\%$ solid phase formed) and the point at which the liquid films transformed into droplets ($\sim 94\%$ solid phase formed) [50]. Another worth mentioning criterion is the hot cracking sensitivity (HCS) proposed by Clyne and Davis [142], in which the relative time interval rather than the temperature interval spent by the mushy zone is used as the index. Based on a similar argument but also taking into account the shrinkage contribution and then the tensile deformation applied perpendicular to the dendrite growth direction, Rappaz et al. [143] introduced the critical deformation rate as the indicator to characterize the HCS. This type of analysis has been adapted for developing LPBF superalloys, for example, the hot cracking resistance has been successfully increased in an LPBF CM247LC after removing the Hf by Griffiths et al. [144], attributed to a narrow solidification range of the Hf-free composition.

Since 2015, Kou and the co-authors published a series of work on predicting the solidification crack susceptibility in castings and welds [145–149]. In Kou's model, columnar dendritic grains were considered. There are three factors: 1. The tensile strain perpendicular to the columnar grains tear them apart and lead to crack; 2. The growth of grains leaning towards each other resists cracks opening; 3. Enough liquid feeding along the interdendritic interface prevents cracking. Based on these arguments, a crack susceptibility index (CSI) has been proposed and mathematically expressed as $|dT/d(f_s)^{1/2}|$, where it describes the absolute value of the derivatives of solidification temperature over the square root of solid fraction, thus the 'steepness' on the T vs $f_s^{1/2}$ curve. In the original form [145], the solid fraction was suggested in the range of 0.87-0.94 for Al-Cu binary alloys. In recent years, CSI

has been successfully implemented to interpret the cracking susceptibility of LPBF Al alloys [150] and Ni alloys [139].

Another model that is worth mentioning here is proposed by Neil Harrison [151]. The ‘processable’ nature of an alloy depends on Thermal Shock Resistance (TSR). Derived from the definition of TSR, Harrison [152] proposed the crack susceptibility of an alloy, χ , as the ratio between the ultimate tensile strength of the alloy σ_{UTS} , or yield strength for ductile materials, and the thermal stress, which is a function of temperature σ_T . By tuning the concentration of significant solid solution strengthening elements to increase the σ_{UTS} value, while the σ_T is presumable un-influenced, Harrison successfully printed modified Hastelloy X with 65% reduced cracks to the original form during LPBF.

4.1 Cracking behavior of nickel-based superalloy in LPBF

The general cracking modes in LPBF nickel-based superalloys can be presented in Fig. 4.1, from an as-LPBF-processed MAD542 superalloy using unoptimized printing parameters, which has a high energy density for this alloy to induce different types of cracks. Generally, the cracks are closely parallel to the building direction presenting the representative feature of hot-tearing cracks. This type of crack is formed at the last stage of solidification before the solid phase is fully developed. The tensile stresses normal to the cracking direction tear the remained liquid phase apart. As in Fig. 4.1(b1), the solidification dendrite arms are commonly found in the crack cleavage, which is known as reliable evidence of solidification cracking [139,153]. The width of the hot-tearing cracks is in the length scale of several micron meters.

After solidification, the solid part would be influenced by the intrinsic heating effect from the laser fusion of the adjacent layer (upper layer). If the heating temperature exceeds the solidus temperature of the solid, localized liquification occurs. Generally, the interdendritic region shows a lower solidus temperature than the dendrite core. This localized liquification region results in cracking with the assistance of tensile stress. The length dimension of the width of these cracks is in the sub-micron scale (see Fig. 4.1(d1)). The remelted liquid film feature is shown in the channel of this type of crack. In the solid part and further away from the heating source, e.g., Fig. 4.1(d2) region in Fig. 4.1(d), sharp crack tips are observed. In this colder region in Fig. 4.1(d2) (comparing with Fig. 4.1(d1)), it may not be liquified. The crack could propagate from the upper liquified region (Fig. 4.1(d1)) into the lower solid region (Fig. 4.1(d2)), leading to the decreasing of the crack width. It should be mentioned that, at the crack tip (Fig. 4.1(d2)), the length dimension of solid-state crack is in the nanometer scale.

In addition, those cracks are observed at the high angle grain boundaries. As documented by Hariharan et al. [153], cracks are occurring along the high-angle GBs with misorientation angles greater than 15° , but in contrast, no crack was found at the low-angle GBs in an LPBF IN738LC superalloy. This phenomenon can be evident in manuscript IV. In the LPBF processed superalloy, most of the grain boundaries are solidification grain boundaries (SGBs), which was originally defined in the welding community [154]. The SGBs

have both a compositional and crystallographic component [154]. Compositionally, the SGB are enriched with interdendritic segregating elements. Crystallographically, the SGBs develop certain misorientations. Besides SGB, another type of grain boundary is migrated grain boundary (MGB). On some occasions, a SGB can migrate away from the interdendritic region carrying the crystallographic component. In this sense, the regions of SGBs, which are equivalent to interdendritic regions, are vulnerable to cracking.

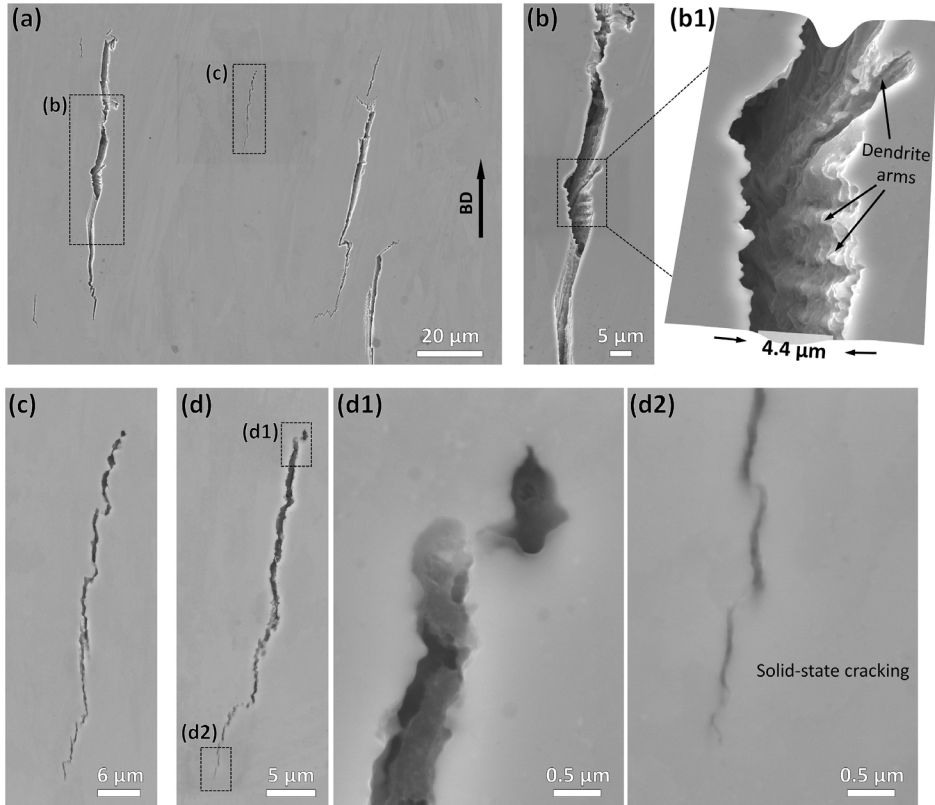


Fig. 4.1. Different types of microcracks observed in as-LPBF-processed superalloy using unoptimized printing parameters from SEM-SE imaging, (a) overall viewing of micro-cracks (b) enlarged view of a hot-tearing type crack, (b1) stereo micrograph indicates the dendrite arm features in the hot-tearing crack cleavage, (c-d) mixed type cracks, (d1) enlarged viewing of the liquid-state cracking feature at the starting region of the micro-crack shown in (d), and (d2) enlarged viewing of the solid-state cracking feature at the ending region. (The building direction (BD) is from bottom to top for all the micrographs).

Owing to the rapid heating and cooling of the LPBF process, the formation of γ' precipitates has been highly suppressed. The absence of γ' in the γ' -strengthened nickel-based superalloy in the as-LPBF-processed condition has been confirmed by synchrotron X-ray diffraction for ABD-900AM [155], STEM micrograph for IN738LC [18], TEM micrograph for Haynes 282 [156], and APT analysis for MAD542 (in manuscript IV). In contrast, some literature has reported the observation of the γ' phase in the as-built microstructure, particularly in LPBF CM247LC [157,158]. Wang et al. [157] observed γ/γ' eutectic from dark-field TEM micrograph. The occurrence of γ/γ' eutectic is along the interdendritic region where the γ' forming elements are enriched. In the eutectic regions, the volume fraction of γ' is approximately 1.5%, according to the statistical determination from Wang et al. [157]. In addition, Divya et al. [158] observed very fine γ' in the as-built CM247LC superalloy from the Moiré fringes of high-resolution TEM micrograph, where the very fine γ' precipitates are approximately 5 nm in diameter. This is likely attributed to 1) the different detailed thermal history during the LPBF process and 2) the high propensity of γ' formation of CM247LC superalloy which has a very high equilibrium γ' volume fraction in the range close to 67%.

In this sense, the SAC and DDC, which are the conventional cracking mode in the welding process, are not the principal considerations for the in-process cracking during the LPBF process.

4.2 Concept of HR-DR model

Here, in this study, the cracking modes for nickel-based superalloy during the LPBF process are defined as (1) liquid-state cracking and (2) solid-state cracking. For liquid-state cracking, the mismatch of the solidification steps of the dendrite and interdendritic regions is the critical consideration. For an alloy where the dendrite and interdendritic regions keep the identical solidification pace, this alloy is less likely to be cracked. This statement could also be interpreted as the liquation cracking susceptibility. The liquation cracking occurs owing to the lower solidus point in the interdendritic region, which induces liquation. If the interdendritic region has a solidus temperature close to the dendrite core, the liquation would not be induced. Regarding solid-state cracking, it is caused by the poor deformation resistance within the interdendritic region which appears as the weaker region where crack propagation occurs.

Two factors, heat resistance (HR) and deformation resistance (DR), are compared between the dendrite core (DC) and interdendritic region (ID). For an alloy whose ID simultaneously obtains the greater HR and DR, this alloy is supposed to simultaneously show higher liquid-state and solid-state cracking resistance.

To formulate the HR-DR model into the mathematic form, the first step is to assign the given composition into the ID and DC species, the second is to calculate the DR and HR values separately for ID and DC, and the last step is comparing the differences of DR and HR between the ID and DC. The working flow is shown in Fig. 4.2. The detailed working procedures and the relevant assumptions are documented in detail in manuscript IV.

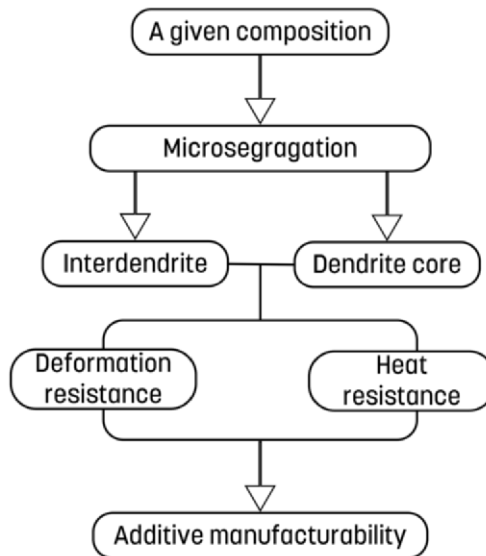


Fig. 4.2. Flow chart of HR-DR model.

4.3 Additive manufacturability diagram

To visualize the HR-DR model, the additive manufacturability diagram of nickel-based superalloy is developed, where the two merit indices are assigned on the X and Y-axis in an X-Y plot, as illustrated in Fig. 4.3. In the diagrams, more than 20 different nickel-based superalloys and their derivative versions [9,18,19,77,139,144,158–187], newly developed γ' -strengthened superalloys [139,155,188,189], experimental nickel-based superalloys [190], and Co-Ni-based superalloys [191], all fabricated by the LPBF process are integrated by implementing their chemical composition including both major and minor alloying elements. As can be seen, the reported cracking conditions in the as-LPBF-processed state correlate very well with the additive manufacturability diagram.

Superalloys that are expected to be readily adapted for the LPBF process are expected to lean towards the top right of the diagram. The additive manufacturability boundary can then also be plotted. As shown in Fig. 4.3(a), the cracked and crack-free superalloys by LPBF are separated by a clear boundary. It should be pointed out here, that the additively manufacturable superalloys are estimated conservatively since the cracking could be caused by un-properly optimized printing parameters. Here a mathematic criterion, the one-dimensional HR-DR index was proposed, as expressed as: $0.7 \cdot \Delta\sigma_{ss} + \Delta T_s = -140$, by using the dimensionless quantities. The utilization of HR-DR index will be explained in 4.4 Validation of HR-DR model.

The superalloys have relied on the minor elements for decades, and these minor elements will be needed to accomplish high-performing superalloys also in the foreseen future. From the AM perspective, these minor elements indeed influence the additive manufacturability in different ways. According to Fig. 4.3(b), Hf, B, and Zr are shown to have the most detrimental effect on the cracking resistance with respect to the liquid-state cracking resistance. The sum of addition of Hf, B, and Zr in at.% is used for coloring the symbols in Fig. 4.3(b). The size of symbols in Fig. 4.3(b) reflects the equilibrium γ' volume fraction calculated at 800 °C (ThermoCalc®, TCNI10 database), which shows less influence on additive manufacturability.

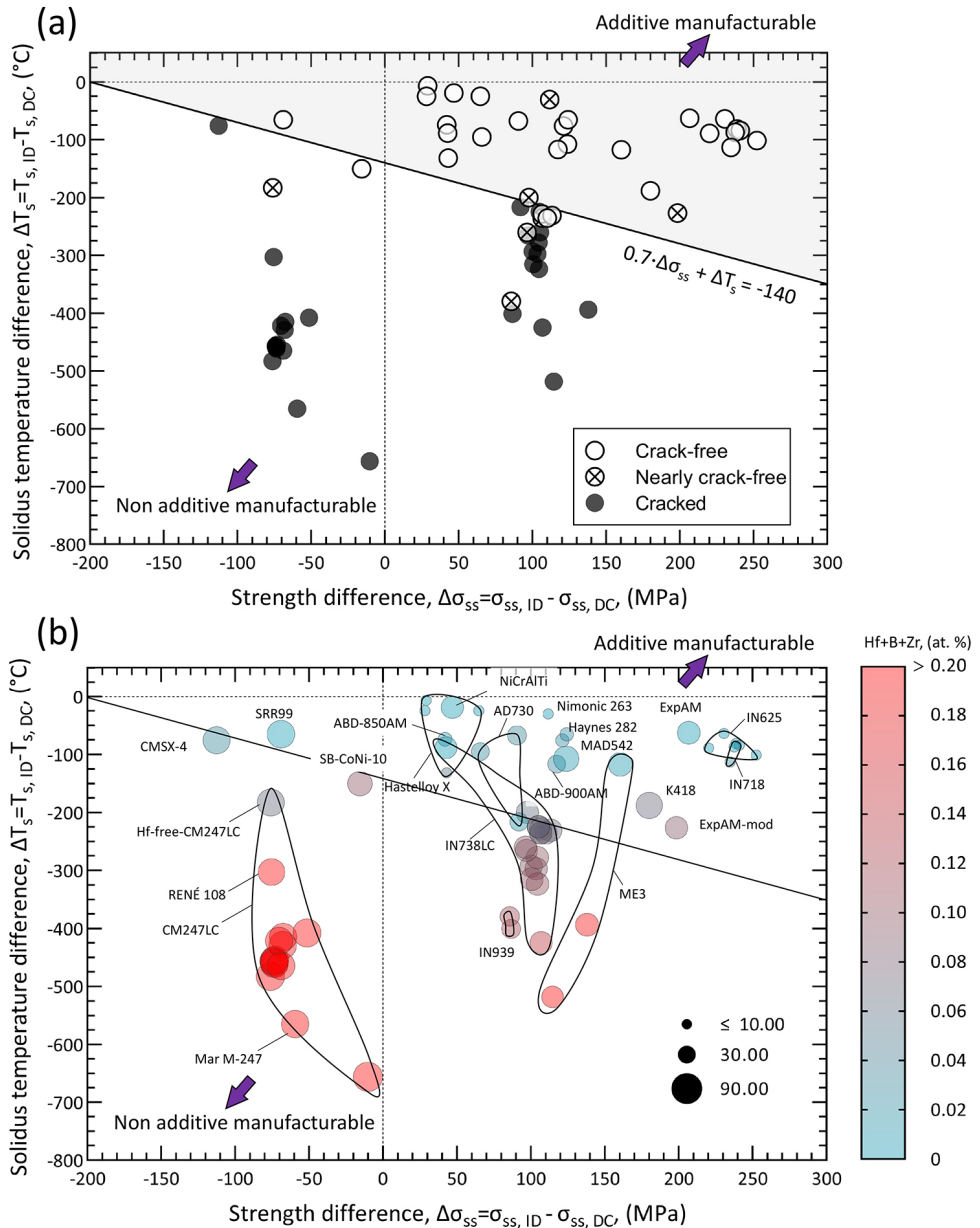


Fig. 4.3. (a) Additive manufacturability diagram of LPBF nickel-based superalloys. In (b), the size of marks indicates γ' volume fraction from thermodynamic calculation at 800 °C, the marks are colored by the addition of the sum of Hf, B, and Zr in at.% according to the color scheme on the right-hand side of (b).

4.4 Validation of HR-DR model

Four IN738LC derivatives, IN738LC-LB/LZr, -HB/LZr, -LB/HZr, and -HB/HZr, with different B and Zr addition, have been used for validation of the HR-DR model. The compositions have been detailed in 3.1 Materials. All the IN738LC derivatives have been fabricated by LPBF using the DoE matrix to explore the optimized printing parameters with the minimum defect level. The crack density has been defined as the length of the crack in a unit area in the unit of (mm/mm²) from the optimized parameters.

According to the counted crack density, IN738LC-LB/LZr shows the lowest crack susceptibility but IN738LC-HB/HZr shows the highest. The locations of the four IN738LC derivatives were mapped in the HR-DR additive manufacturability diagram in Fig. 4.4(a). According to this diagram, IN738LC-LB/LZr and IN738LC-LB/HZr are located at the printable region and the other two are not, showing an excellent agreement between the predicted additive manufacturability and experimental findings. To step further, the measured crack densities have been plotted as a function of the one-dimensional HR-DR index, as illustrated in Fig. 4.4(b). The horizontal and vertical dashed lines indicate the crack density of 0.1 mm/mm² and HR-DR index of -140, which is the boundary shown in Fig. 4.4(a). Based on this plot, to reduce the crack density below 0.1 mm/mm², a minimum HR-DR index of approximately -140 is necessary. Considering the extraordinary prediction of this model, the addition of alloying elements, especially for critical minor elements, can be further modified to fulfill the additive manufacturability demands.

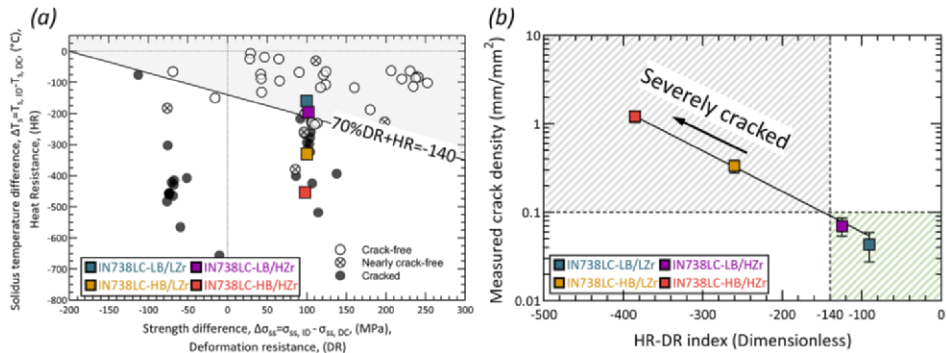


Fig. 4.4. (a) The plot of the four IN738LC derivatives on the two-parameter-based additive manufacturability diagram, and (b) plot of measured crack density as a functional form of single-parameter HR-DR index.

Chapter 5 LPBF and Post-processing

5.1 LPBF manufacturing of MAD542 and Alloy738+

To determine the LPBF processing window of the MAD542 and Alloy738+ superalloy, the same DoE matrix has been used on an EOS M100 LPBF system. The as-built defect checking was carried out using image analysis on the optical micrograph. The plot of defect (including microcracks, porosity, and lack of fusion defects) area fraction as a function of LPBF energy density of MAD542 and Alloy738+ is shown in Fig. 5.1. By using the optimized printing parameters, both MAD542 and Alloy738+ can be processed with limited defects less than 0.1% area fraction.

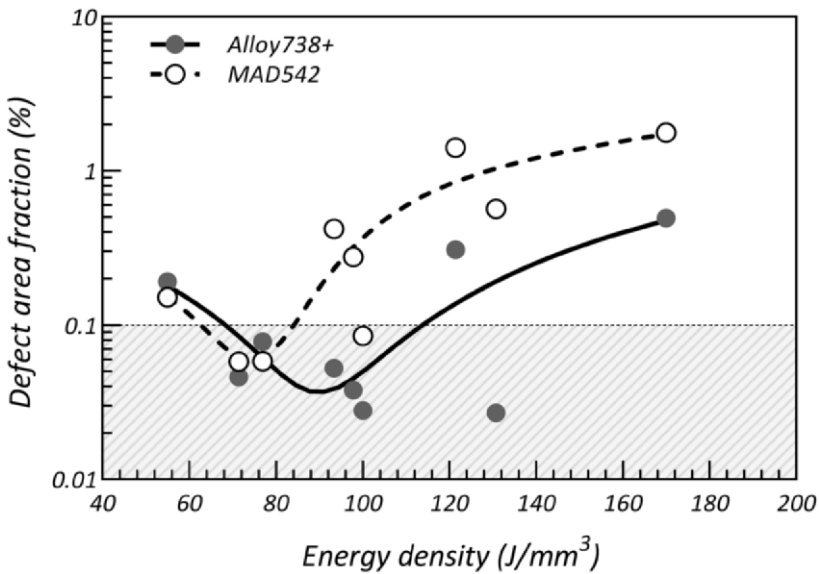


Fig. 5.1. Laser powder bed fusion processing window for MAD542 and Alloy738+.

5.2 Grain structure evolution

In the as-built sample, the preferred grain orientation was found along its <001> orientation parallel to the building direction and establish a strong texture. It has been widely observed in the LPBF processed metals with cubic crystal, such as 316 L stainless steel [67], Aluminum alloy [65], IN738LC [70], MAD542 (manuscript VI), and CM247LC (paper III) superalloys. The post-processing temperature plays a pivotal role in controlling the crystallographic temperature. The maximum values of multiples of a random distribution (M.R.D) in the (200) neutron pole figure as a function of temperature difference have been summarized for LPBF MAD542 and CM247LC in Fig. 5.2. Here, the temperature difference was normalized as the difference between the annealing temperature and the γ' solvus temperature. All the annealing times were 2 h. The γ' solvus temperatures were determined by DSC measurement as 1226 °C for MAD542 [192], and 1250 °C for CM247LC [133].

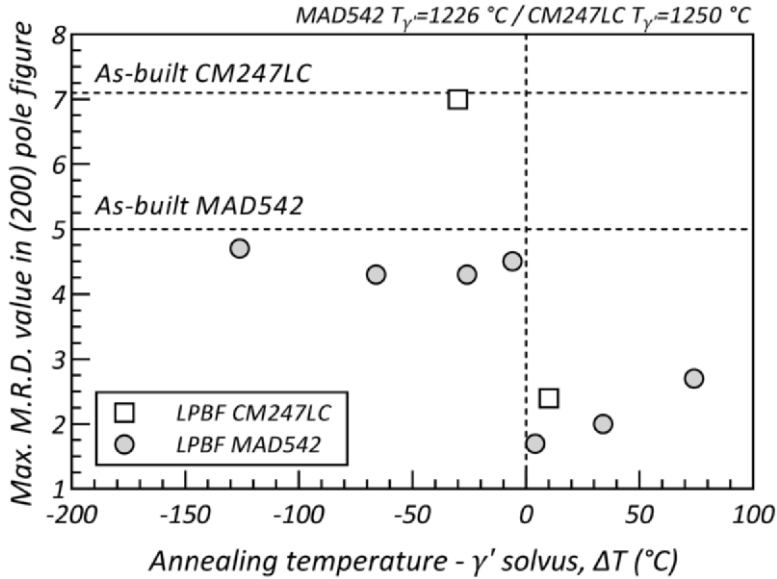


Fig. 5.2. Maximum M.R.D value in (200) neutron pole figures as a function of the temperature difference between annealing temperature and the γ' solvus temperature for LPBF MAD542 and CM247LC superalloy.

With the annealing temperature below the γ' solvus temperature, the texture intensity largely remained at the same level as in the as-built sample for both LPBF superalloys. In contrast, when the annealing temperature is above the γ' solvus temperature, a significant reduction in the intensity of texture can be achieved. It is attributed to the sluggish GB migration owing to the lack of strong difference of stored energy between the adjacent grain area. Additionally, GB Zener pinning effect, acting as a dragging force against the GB migration, is difficultly overcome by the capillary driving force, at the sub-solvus

temperatures. More discussion is referred to in paper III, where the microstructural evolution of an LPBF CM247LC subjected to various post-processing temperatures was systematically investigated.

A discussion is worth bringing up here. In dilute solutions, the grain boundary segregating elements show a large influence on the grain boundary migration kinetics owing to the impurity-drag [193] (also known as solute drag) effect [194]. The migrating grain boundary will leave the grain boundary segregating element behind and then exert attraction force on the solutes to induce them to diffuse towards the migrating boundaries. As a result, this attraction force will act as the dragging force holding back the grain boundary migration [195]. Although the quantitative description of the dragging effect from the possible solute-drag-like approach is not well investigated for the high alloying element system, this phenomenon has been widely reported in the dilute system.

Considering the migrating GBs were originally located at the interdendritic region as SGBs, the interdendritic segregating elements may have a big impact on the GB migration. Fig. 5.3 shows a plot of recrystallized grain size (defined as the square root of grain area) and twin boundary (TB) length fraction vs. the sum of Mo+Nb nominal concentration in at.%. Here the interdendritic segregating elements Mo and Nb are selected as representatives. The detailed post-processing treatments can be found in paper II for MAD542, [18] for IN738LC-M, and paper III for CM247LC. A clear tendency can be observed between grain size/TB fraction and Mo+Nb concentration. With less Mo+Nb (interdendritic elements), coarser grains can be expected, meanwhile less TB was promoted. It is likely attributed to the Strain Induced Boundary Migration (SIBM) mechanism which is accompanied by the formation of annealing twins [196,197].

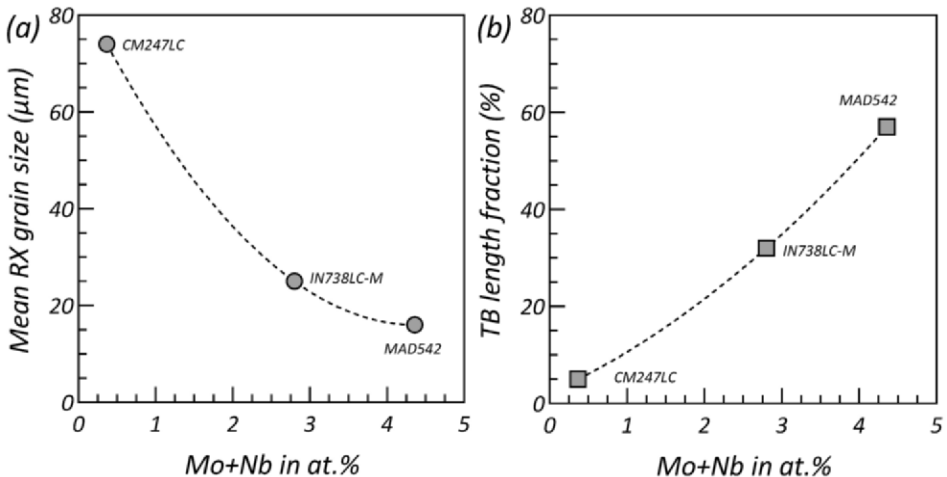


Fig. 5.3. (a) mean recrystallized grain size and (b) twin boundary length fraction as a function of Mo+Nb at.% of LPBF superalloys.

5.3 Effect of post-processing on the precipitates

Like the γ' -strengthened nickel-based superalloy manufactured from the conventional processes, the solution temperature and time play a significant role in controlling the precipitates. An example of the super-solvus treatment of MAD542 superalloy has been illustrated in Fig. 5.4. The heat treatment temperature for solutioning was set at 1230 °C, which is higher than the γ' solvus temperature (1226 °C) and in the single-phase austenitic region of this alloy. The formation of the γ' phase occurs during the cooling process. Another goal of solutioning heat treatment is to achieve a more uniformly dispersed γ' phase. For less duration time at the super-solvus temperature, like 10 and 60 min in Fig. 5.4, coarser γ' were observed aligned along with the interdendritic region, where the γ' formation elements were enriched. This observation is consistent with the coarser γ' observed at the interdendritic region in cast superalloys [198,199].

Although in the literature, a much shorter solution time is enough for completion of the chemical homogenization in additively manufactured superalloy owing to its much finer dendrite arm spacing [22], at least 2-h solution time was used for the heat treatment in this study, according to the observation in Fig. 5.4.

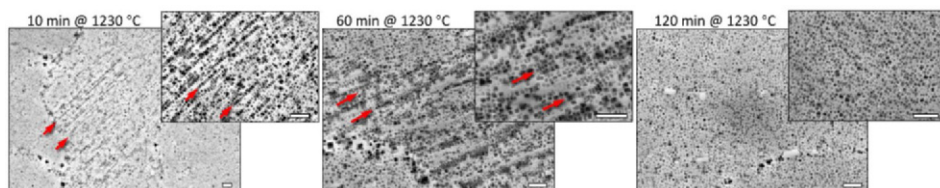


Fig. 5.4. The γ' morphology from secondary electron SEM imaging of solutioning heat-treated MAD542 superalloy for 10 min, 60 min, and 120 min. The samples were prepared by chemical etching. All the scale bars indicate 1 μm .

Chapter 6 Mechanical properties

In this chapter, the mechanical properties of a wide group of LPBF superalloys have been summarized. The mechanical properties include uniaxial tensile properties at room temperature and high temperatures, slow strain rate tensile properties, creep properties and the correlation between SSRT and creep, and the summarized time-dependent properties. For the tensile testing for both at the room temperature and the elevated temperatures, the nominal strain rate is 10^{-3} s^{-1} . The denotations of HB and VB in the figure legends indicate the building directions of the testing bars, where the loading direction is perpendicular (HB) and parallel (VB) to the building direction. The denotations of LPBF superalloys in this chapter and their post-processing treatments information are listed in Table 6.1.

Table 6.1. Denotations and post-processing treatment information of the LPBF superalloys included in this chapter

Materials	γ' solvus	HIP	Solution	Aging #1	Aging #2	
ABD850AM-HT [139,155]	1025 °C	-	980 °C/2h	850 °C/4h	760 °C/16h	
ABD850AM-Mod-HT [139,155]		-	980 °C/2h	850 °C/4h	760 °C/16h	
ABD900AM-HT [139,155]	1079 °C	-	1050 °C/2h	850 °C/4h	760 °C/16h	
Alloy2-Subsolvus-aging [76]	1182 °C	-	1100 °C/4h	850 °C/20h	-	
Alloy2-Supersolvus-double aging [76]		-	1220 °C/2h	1100 °C/4h	850 °C/20h	
Alloy738+ 1230 °C/2h+aging	1176 °C	-	1230 °C/2h	850 °C/24h	-	
Alloy738+ 1260 °C/2h+aging		-	1260 °C/2h	850 °C/24h	-	
Alloy738+ 1200HIP+Aging		1200 °C/4h	-	850 °C/24h	-	
Alloy738+ 1200HIP		1200 °C/4h	-	-	-	
Alloy738+ 1230HIP+Aging		1230 °C/4h	-	850 °C/24h	-	
Alloy738+ 1230HIP		1230 °C/4h	-	-	-	
CM247LC-HIP+HT [188]		1249 °C	1260 °C/2h	-	1079 °C/4h	871 °C/20h
CM247LC-HT [139,155]		1250 °C	-	1260 °C/2h	1079 °C/2h	871 °C/20h
ExpAM-HIP+HT [188]	1235 °C	1260 °C/2h	-	1079 °C/4h	871 °C/20h	
ExpAM-Mod-HIP+HT [188]	1212 °C	1260 °C/2h	-	1079 °C/4h	871 °C/20h	
IN738LC-1-1210 °C HIP+SHT	1148 °C	1210 °C/4h	1120 °C/2h	850 °C/24h	-	
IN738LC-2 1210HIP+SHT		1210 °C/4h	1120 °C/2h	850 °C/24h	-	
IN738LC-7-1210 °C HIP+SHT		1210 °C/4h	1120 °C/2h	850 °C/24h	-	
IN738LC-E-1200 °C HIP+SHT		1200 °C/4h	1120 °C/2h	850 °C/24h	-	
IN738LC-M-1000 °CHIP+SHT		1000 °C/4h	1120 °C/2h	850 °C/24h	-	
IN738LC-M-1210 °CHIP+SHT		1210 °C/4h	1120 °C/2h	850 °C/24h	-	
IN738LC-HB/HZr 1210HIP+SHT		1210 °C/4h	1120 °C/2h	850 °C/24h	-	
IN738LC-HB/LZr 1210HIP+SHT		1210 °C/4h	1120 °C/2h	850 °C/24h	-	
IN738LC-LB/HZr 1210HIP+SHT		1210 °C/4h	1120 °C/2h	850 °C/24h	-	
IN738LC-LB/LZr 1210HIP+SHT		1210 °C/4h	1120 °C/2h	850 °C/24h	-	
IN939-HT [139,155]		1088 °C	-	1160 °C/2h	1000 °C/4h	850 °C/16h
MAD542 SubA		1226 °C	-	1160 °C/2h	900 °C/24h	-
MAD542 SubNA	-		1160 °C/2h	-	-	
MAD542 SuperA	-		1230 °C/2h	900 °C/24h	-	
MAD542 SuperNA	-		1230 °C/2h	-	-	

6.1 Room-temperature tensile properties

The room-temperature properties of LPBF superalloys have been demonstrated in Fig. 6.1, as plotted as the yield strength vs elongation at fracture. For comparison, the tensile results of vertically built IN718 [200] and horizontally built IN738LC (IN738LC-M) [18] in the as-built condition and with various post-processing treatments have been included. A general trade-off relationship between strength and ductility can be established among these LPBF superalloys. There are some results that can be highlighted. Firstly, the HIP cycle was found beneficial for enhancing the ductility by comparing the IN718-AB-VB and IN718-HIP-VB, where the yield strengths are found at the same level while a significant improvement of ductility was observed (Fig. 6.1(a)). Secondly, the as-built IN738LC superalloy displays a good combination of strength and ductility than the post-processing treated samples, owing to the strengthening effect from the high dislocation density (Fig. 6.1(b)). Thirdly, the newly developed AM superalloys show a close room-temperature yield strength in the range of approximately 900-1100 MPa, whilst the elongation at fracture varies largely from approximately 1-25% engineering strain (Fig. 6.1(d)). Additionally, surprising embrittlement at room temperature was found for MAD542 SuperA-VB, Alloy738+ HB samples (Fig. 6.1(d)). What is in common is that these samples have undergone a super-solvus solution treatment and the following aging step.

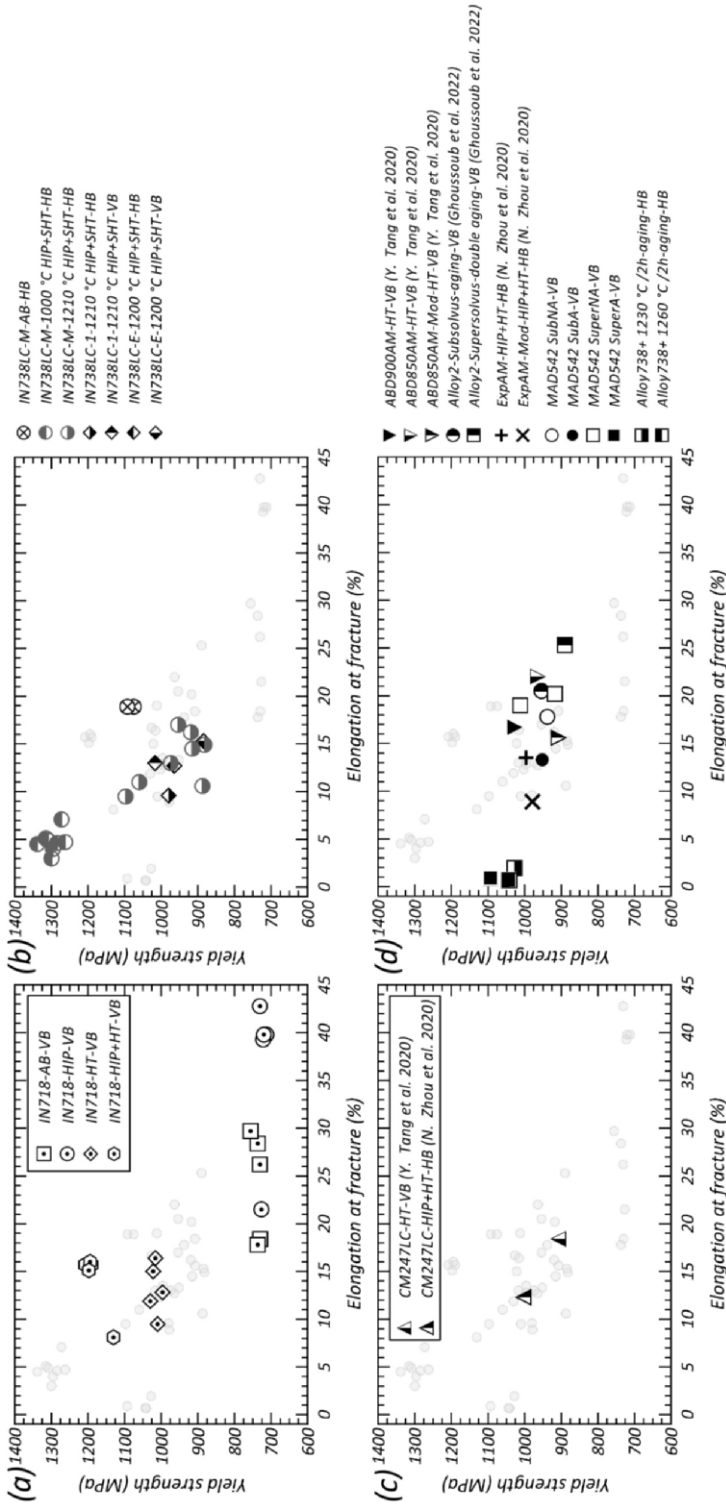


Fig. 6.1. Summarized tensile property of LPBF fabricated superalloys at room temperature (a) IN718 [200], (b) IN738LC [18], (c) CM247LC, and (d) newly developed AM superalloys.

6.2 High-temperature tensile properties

The tensile properties of the LPBF superalloys at the elevated temperatures have been summarized in Fig. 6.2, where (a-c) and (d-f) present the yield strength and elongation at fracture as a function of temperature, respectively. Among IN738LC, CM247LC, and IN939 (Fig. 6.2(a)), IN939 shows an obvious lower yield strength than the others owing to its relatively low γ' volume fraction. Above 800 °C, the significant drop of yield strength can be found in both IN738LC and CM247LC specimens. While CM247LC shows a slightly higher yield strength than IN738LC, but meanwhile, the relatively lower ductility can be found for the high-strength superalloy CM247LC in Fig. 6.2(d). For the newly developed superalloys found in literature (Fig. 6.2(b)), the high-temperature strength is varying within the strength range close to the heritage grades in Fig. 6.2(a). Among them, Alloy2 specimens show the overall highest yield strength, while the elongation at fracture for sub-solvus and super-solvus treated Alloy2 are far different (Fig. 6.2(e)), although the yield strength is close to each other. For new superalloys in this study, both MAD542 and Alloy738+ are in the highest yield-strength range as presented in Fig. 6.2(c). However, except for the sub-solvus treated MAD542, all the super-solvus treated MAD542 and Alloy738+ show nearly no elongation at fracture (Fig. 6.2(f)). Similar to the loss of ductility of super-solvus treated Alloy2, the super-solvus treated Alloy738+ and MAD542 superalloys also display this behavior. It is believed that the super-solvus treatment triggers the grain boundary embrittlement to a large extent for LPBF high-strength superalloys. Regarding this topic, more characterization and discussion are included in the appended manuscript VI.

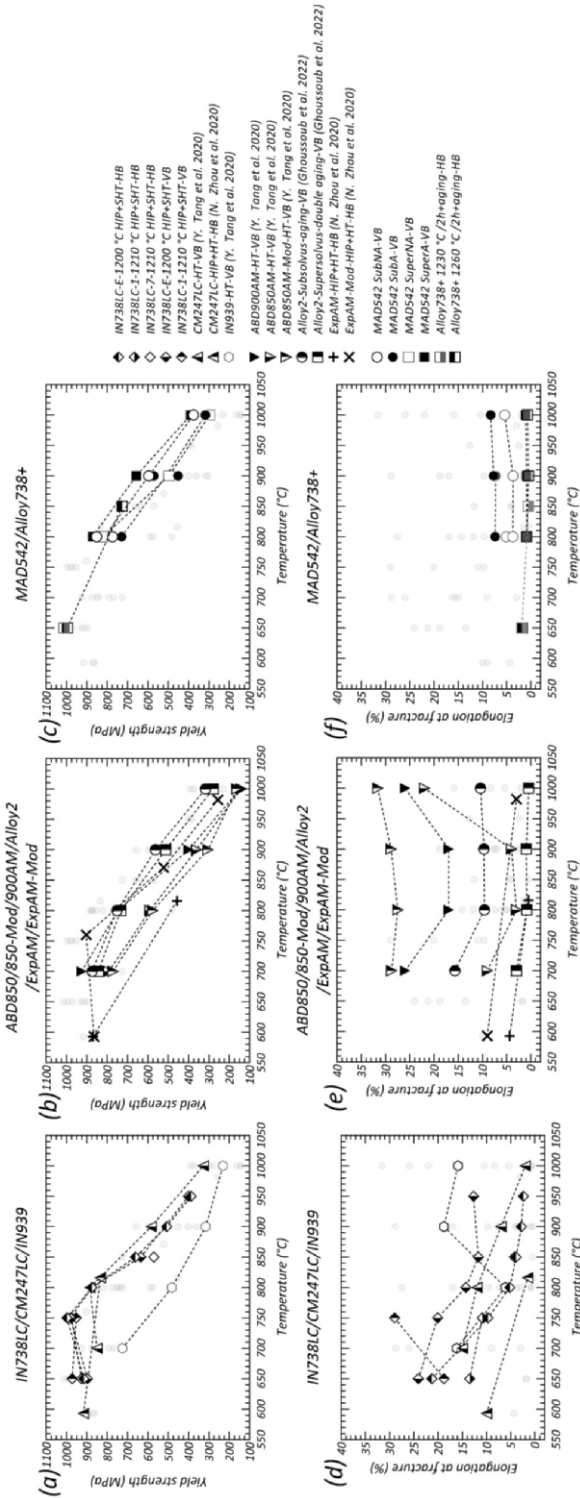


Fig. 6.2. Summarized tensile property of LPBF superalloys at the elevated temperatures, (a) yield strength and (d) elongation as a function of temperature for LPBF IN738LC/CM247LC/IN939 superalloys; (b) yield strength and (e) elongation as a function of temperature for LPBF ABD850/850-Mod/900AM/Alloy2/ExpAM/ExpAM-Mod superalloys; (c) yield strength and (f) elongation as a function of temperature for LPBF MAD542/Alloy738+ superalloys.

6.3 High-temperature slow strain rate tensile testing

The slow strain rate test was originally developed in the 1960s for evaluating the environmental-assisted damage by applying the slow dynamic strain at a constant extension rate in the environment of interest [201]. In this study, slow strain rate tensile (SSRT) testing was conducted in the high-temperature environment with lab air, for assessing the short-term creep performance of additively manufactured nickel-based superalloy. To distinguish the SSRT from the conventional tensile testing, the corresponding constant strain rate of SSRT is in the range from 10^{-4} to 10^{-7} s^{-1} according to the standard [202].

Fig. 6.3 shows the SSRT engineering stress-strain curves of LPBF IN738LC-2 superalloys fabricated as horizontally built (a) and vertically built (b) specimens. More SSRT testing results are referring to the references for MAD542 [189], IN738LC-(LB/LZr; LB/HZr; HB/LZr; HB/HZr) (manuscript V), and IN738LC-7 (paper I [71]). For both building directions, a clear strain rate-dependent flow stress response can be found, where the flow stresses decrease with the decreasing strain rates. Meanwhile, the anisotropic mechanical properties are noted between the HB and VB specimens, where VB illustrates both higher flow stress and ductility (except for strain rate at 10^{-7} s^{-1}) than HB.

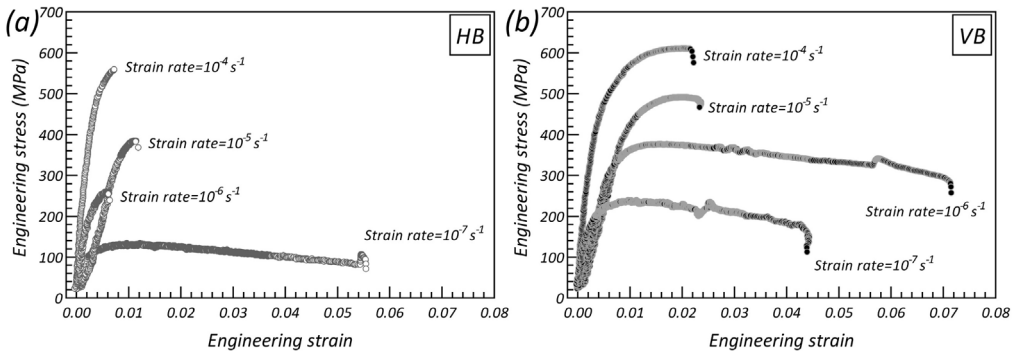


Fig. 6.3. SSRT engineering stress-strain curves for the (a) HB and (b) VB LPBF IN738LC-2 superalloys tested by constant displacement rate control at $850 \text{ }^{\circ}\text{C}$.

6.4 Correction between SSRT and creep

In this study, the IN738LC-2 superalloy has been tested under both SSRT and creep at the identical temperature at $850 \text{ }^{\circ}\text{C}$. For the deformation process, typical dynamic constitutive equations were expressed as power-law equations, namely $\sigma = C\dot{\epsilon}^m$ or $\dot{\epsilon} = C'\sigma^n$, where C and C' are materials constants, $\dot{\epsilon}$ is the strain rate and σ is the flow stress, m is the strain rate sensitivity, and n is the stress exponent. And the product of m and n is equal to unity. Fig. 6.4 shows the plots of the relations between flow stress and strain rate. For SSRT, the maximum flow stress, σ_t and the corresponding tensile strain rate $\dot{\epsilon}_t$ were used, while for creep, the applied stress σ_a and minimum creep rate $\dot{\epsilon}_{min}$ was used. As shown in the figures,

for both HB and VB samples, the SSRT and creep results were correlated well in both the strain rate sensitivity and stress exponent-based analysis. The products of $m \times n$ were calculated very close to 1, as 0.951 and 0.970 from the curve fitting for HB and VB samples, respectively.

Prasad et al. [203] originally proposed a dynamic materials model considering the testing rig as the source of power and the testing piece as a dissipator of power. In the model, the total input power per unit volume, P_v , is expressed as the product of the flow stress (effort) σ , and strain rate (flow) $\dot{\epsilon}$, as $P_v = \sigma \cdot \dot{\epsilon}$. The P_v is attributed to two parts: 1) the temperature rise and 2) the metallurgical evolution as the overall result of dynamic recovery, dynamic recrystallization, cavity formation/growth, precipitates evolution, deformation-induced phase transformation [203]. This analysis approach has been successfully applied to the optimization of the processing window during thermomechanical processing for a wide group of metallic materials [204–206]. In this study, for the correlation between SSRT and creep testing, the assumption is that the total input power per specific volume is the same for the identical material tested at the identical temperature at the identical strain rate or flow stress. In the following section, 6.6 Summarized time-dependent performance, the SSRT and creep results are compiled together in this manner.

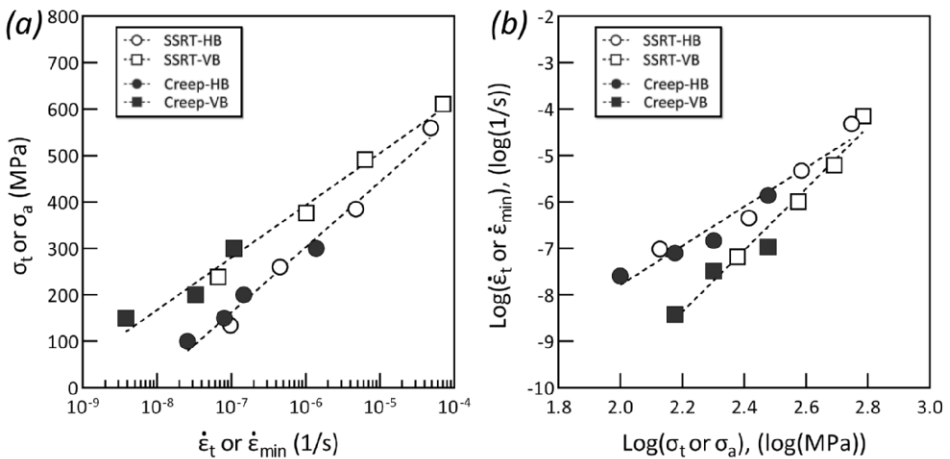


Fig. 6.4. Correlation between SSRT and creep, (a) max. flow stress in SSRT or applied stress in creep as a function of the corresponding SSRT strain rate or min. creep rate in the semi-log coordinate, (b) logarithmic of SSRT strain rate or min. creep rate as a function of the corresponding logarithmic of max. flow stress in SSRT or applied stress in creep. The test temperature was 850 °C.

6.5 Creep property of LPBF superalloys

The creep curves of the tested LPBF superalloys in this work have been demonstrated in Fig. 6.5, in the manner of strain vs. creep time. Multiple materials have been tested

including heritage grades like IN738LC and CM247LC and new LPBF superalloys like MAD542 and Alloy738+. The samples were fabricated from two different directions: HB and VB, where the loading direction is perpendicular and parallel to the loading direction. The tested temperatures are in the range of 850-900 °C, and in most cases are 850 °C.

For the same superalloy fabricated from the different building directions, VB specimens display a much longer creep rupture life than the HB specimens. In addition, from the shape of the creep curve, the tertiary creep regime in VB specimens develops to a greater extent than HB samples. For the tertiary creep, the rate-controlling factor is the instability of microstructure, e.g., initiation of cracks from linked creep voids, the creep rate is accelerated till rupture [207]. For the HB specimens of CM247LC and MAD542, even sudden fracture can be observed from the creep curve where nearly no tertiary creep can be found.

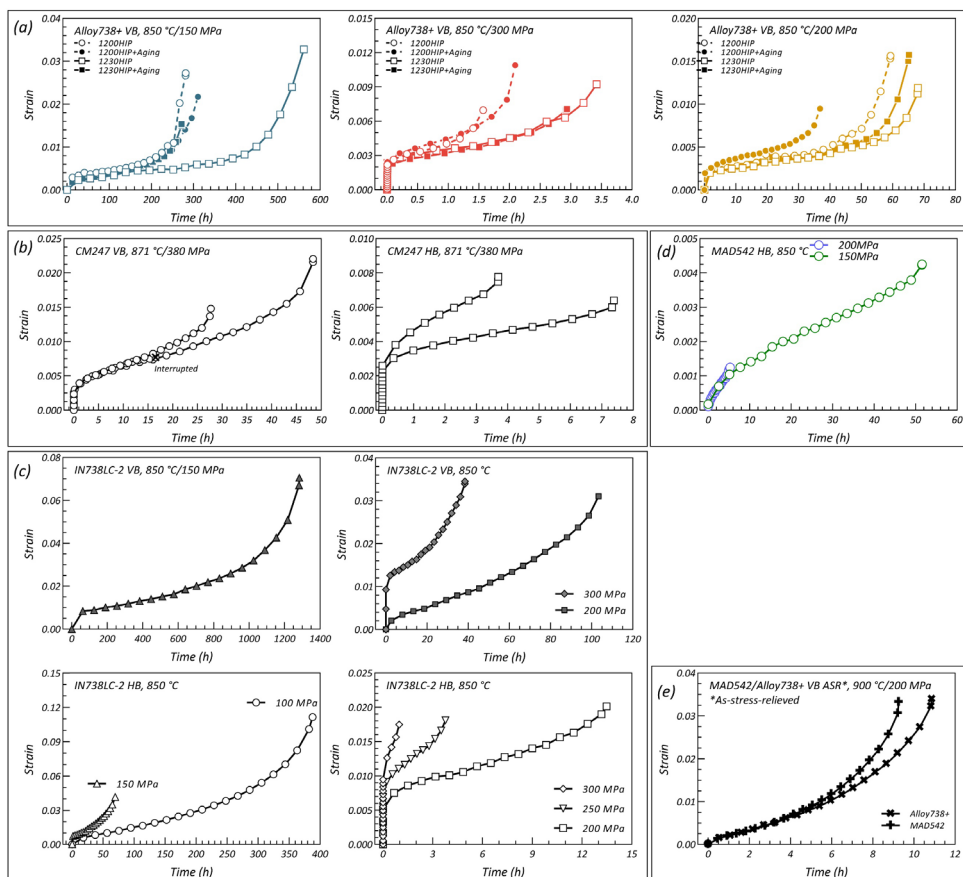


Fig. 6.5. Strain vs. time creep curves of the tested LPBF superalloys in this study, (a) Alloy738+ tested at 850 °C, (b) CM247LC superalloy tested at 871 °C, (c) IN738LC-2 superalloy tested at 850 °C, (d) MAD542 superalloy tested at 850 °C, and (d) MAD542 and Alloy738+ superalloys tested at 900 °C.

The creep performances of the tested LPBF superalloys have been plotted in the Larson-Miller diagram with the comparison of a LPBF superalloy from the literature and the cast superalloys, shown in Fig. 6.6. Among the selected materials, CM247LC in the DS form undoubtedly shows the greatest creep properties in the full stress range in this plot. Then, cast Mar-M-247 and cast IN738 superalloys also present excellent creep properties. Among the LPBF superalloys, the VB CM247LC specimens show marginally better creep properties than the cast IN738 at 380 MPa (tested at 871 °C), while the HB specimens are worse than the average of cast IN738. However, for the LPBF IN738LC superalloys, the VB specimens show an approximately one order of magnitude shorter rupture life than the cast ones, and then the HB specimens show approximately two orders of magnitude shorter rupture life than the VB specimens. The superalloys, MAD542 HB specimens show an inferior creep performance than the IN738LC-2 HB specimens. And Alloy738+ VB specimens demonstrate a creep performance between the IN738LC-2 VB and HB samples. It should be noted here that these heat treatments on Alloy738+ decreased the creep performance of this alloy, where a larger value of LMP was found for the Alloy738+ LPBF VB ASR, where ASR indicates as-stress-relieved at 600 °C for 20 h.

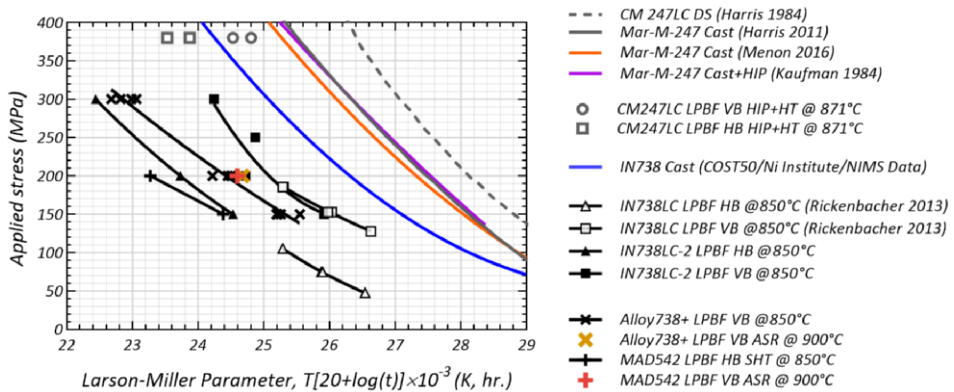


Fig. 6.6. Larson-Miller plots of the tested LPBF superalloys with a comparison with LPBF IN738LC [32], cast IN738, cast Mar-M-247 [126–128], and directionally solidified CM247LC [125].

6.6 Summarized time-dependent performance

The time-dependent deformation performance of the tested LPBF superalloys in this study is summarized in Fig. 6.7. The testing temperature is 850 °C. For comparison, the creep performance of cast IN738 at 850 °C is included in the plots. The minimum deformation rate vs applied stress of HB and VB specimens were shown in Fig. 6.7(a) and (c), respectively, and the elongation at fracture vs applied stress was shown in Fig. 6.7(b) and (d), respectively. Comparing between HB and VB of LPBF superalloys, the VB specimens demonstrate an overall greater deformation resistance and longer elongation at fracture. Comparing the IN738 from the LPBF and cast process, the LPBF IN738LC shows an apparently inferior creep performance than the cast counterparts. Even for the VB LPBF IN738LC, the minimum deformation rate is approximately 5-10 times faster than the cast IN738 (Fig. 6.7(c)) and the elongation at fracture is comparable to the lower boundary of cast IN738 data (Fig. 6.7(d)). Referring to the newly developed superalloys, the HB MAD542 shows a better minimum deformation resistance rate than the HB IN738LC serials (Fig. 6.7(a)). However, the marginally better creep resistance was exchanged by the large ductility loss (Fig. 6.7(b)). A similar trend has been found for VB Alloy738+ specimens, where their minimum deformation resistance rates are within the same level of VB IN738LC (Fig. 6.7(c)), while the values of elongation at fracture are approximately 1/3 of the VB IN738LC fractured at the accordingly identical applied stress (Fig. 6.7(d)). The reduced creep ductility of MAD542 and Alloy738+ superalloys is associated with the lack of ductility from the tensile testing at the nominal strain rate of 10^{-3} s^{-1} shown in 6.2 High-temperature tensile.

Additionally, as detailed in Paper I, the deformation mechanism and fracture mechanics during short-term creep deformation of LPBF γ' -strengthened superalloy is attributed to the dislocation activity assisted grain boundary shearing induced intergranular cracking. The minimum strain rate of nickel-based superalloys during creep at the intermediate temperature can be formulated as the additive summation of rate terms of dislocation creep and grain boundary sliding [208]. The dislocation creep rate part is dependent on the size and morphology of γ' , volume fraction and inter-spacing of γ' precipitates, and the diffusivity of γ matrix for the necessary dislocation climb within the bulk grain [209]. Assumably, the HB and VB IN738LC-2 have the close contributions of dislocation creep rates to the overall creep rates, owing to the close γ and γ' characteristics. Then the minimum deformation rate difference between these two specimens is attributed to the difference from the corresponding grain boundary sliding rates. Furthermore, the premature intergranular fracture is supposed to be responsible for the faster strain rate and lower elongation at fracture for the LPBF superalloys compared to the casting specimens.

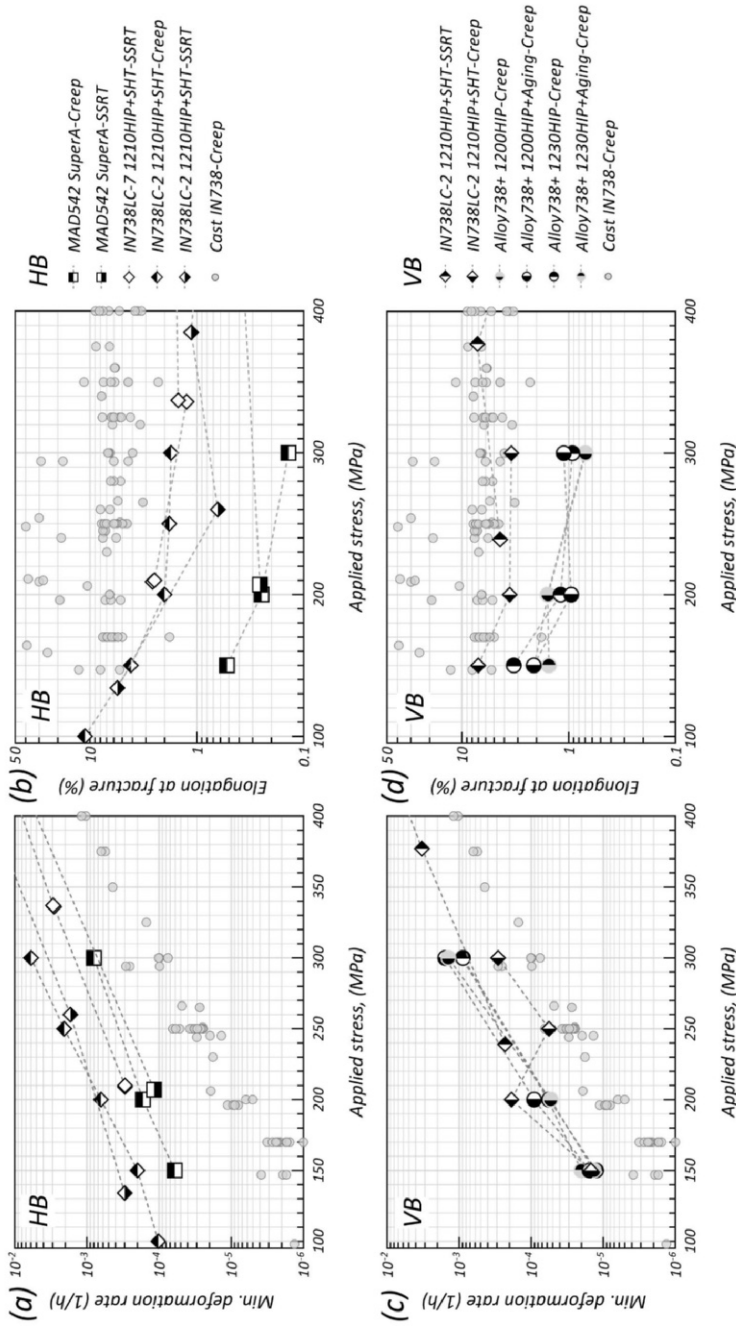


Fig. 6.7. Summarized time-dependent performance at 850 °C of LPBF superalloys (a) minimum deformation rate as a function of applied stress for horizontally built specimens, (b) elongation at fracture as a function of applied stress for horizontally built specimens, (c) minimum deformation rate as a function of applied stress for vertically built specimens, (d) elongation at fracture as a function of applied stress for vertically built specimens.

Chapter 7 Oxidation property

The oxidation property of a wide group of LPBF, cast, SX, and PM superalloys are summarized as presented as the parabolic rate constants vs. oxidation temperature shown in Fig. 7.1. The parabolic rate constant K_p value was linearly fitted as the slope from the square of weight gain vs oxidation time curve. Parabolic rate constant K_p is initially proposed by Wagner, to formulate the diffusion-based parabolic kinetics [210]. The specific weight change curve as a function of time is presented in manuscript VII. All the K_p values have been normalized into the unit of $(\text{mg}/\text{cm}^2)^2/\text{h}$. The numerical values are summarized in Table 7.1.

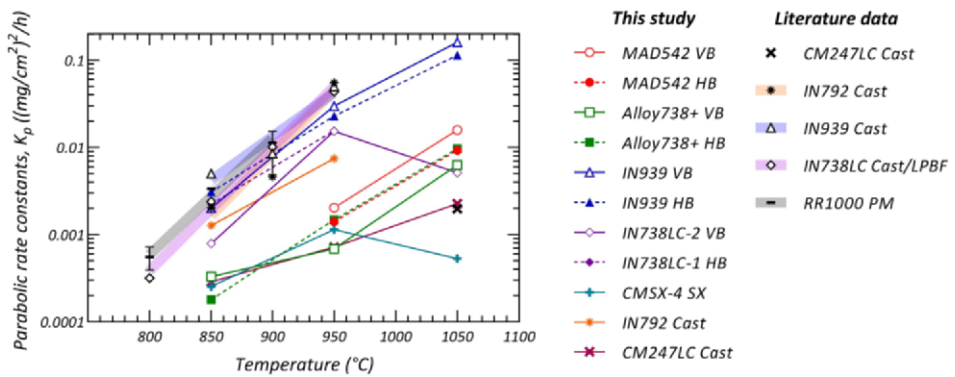


Fig. 7.1. Oxidation resistance in terms of parabolic rate constants.

For all the alloys in Fig. 7.1 except for IN738LC-2 VB and CMSX-4 SX, the K_p values increase with increasing the oxidation temperatures. The drop of K_p indicates the formation of different dominated oxide layers at that temperature. The LPBF and cast versions of the same grade of superalloys, such as LPBF IN939 and IN738, share a close K_p value at the same oxidation temperature. At 850 °C and 950 °C, LPBF Alloy738+ shows a significantly greater oxidation resistance than the parent alloy IN738LC in both LPBF and castings and is comparable to the cast CM247LC and SX form CMSX-4. The new LPBF superalloy MAD542 also shows very good oxidation resistance at 950 °C. However, at an even higher temperature at 1050 °C, the superiors of CM247LC cast and CMSX-4 SX are obvious, both Alloy738+ and MAD542 could not effectively establish reliable oxidation resistance at this temperature.

Table 7.1. Summarized parabolic constants from this study and literature [211–217].

Alloy	Ref.	Parabolic constant, K_p [(mg/cm ²) ² /h]				
		800 °C	850 °C	900 °C	950 °C	1050 °C
MAD542 VB	This study				2.03E-03	1.58E-02
MAD542 HB	This study				1.41E-03	9.23E-03
Alloy738+ VB	This study		3.31E-04		6.87E-04	6.27E-03
Alloy738+ HB	This study		1.80E-04		1.48E-03	9.64E-03
IN939 VB	This study		2.02E-03		2.98E-02	1.61E-01
IN939 HB	This study		3.08E-03		2.28E-02	1.14E-01
IN738LC-2 VB	This study		7.89E-04		1.53E-02	5.14E-03
IN738LC-1 HB	This study		2.25E-03		1.55E-02	
CMSX-4 SX	This study		2.55E-04		1.14E-03	5.30E-04
IN792 Cast	This study		1.27E-03		7.47E-03	
CM247LC Cast	This study		2.87E-04		7.18E-04	2.27E-03
CM247 Cast	(Nowak, 2017)					1.98E-03
IN792 Cast	(Palmert, 2009)		2.03E-03	4.60E-03	5.55E-02	
IN939 Cast	(Palmert, 2009)		4.99E-03	8.52E-03	5.02E-02	
IN738LC Cast	(Mallikarjuna, 2017)			1.00E-02		
IN738LC Cast	(Palmert, 2009)		2.39E-03	1.73E-02	4.35E-02	
IN738 Cast	(Cade, 2014)			8.14E-03		
IN738LC LPBF	(Kim, 2021)	3.17E-04		4.91E-03		
RR1000 PM	(Cruchley, 2013)	4.39E-04	3.36E-03	1.13E-02		
RR1000 PM	(Taylor, 2014)	6.70E-04				

Chapter 8 Conclusions and outlook

8.1 Conclusions

Based on the results presented above, the following conclusions have been drawn, which calls back to section 1.2 Research objectives.

1. To understand the in-process cracking mechanisms for high-strength nickel-based superalloys during the LPBF process. To propose a reliable and easy-to-use cracking susceptibility model for this group of alloys. To propose new superalloys chemical compositions based on additive manufacturability and high-temperature performance indices.

In this work, the cracking mechanisms have been comprehensively reviewed from the literature. Owing to the extremely high cooling rate of the LPBF process, the formation of γ' is highly suppressed, resulting in the cracking occurring in the state of absence of γ' . Based on the understanding of the cracking mechanisms for LPBF of γ' -strengthened nickel-based superalloys, a two-parameters HR-DR model for predicting the additive manufacturability of nickel-based superalloys was proposed. The fundamental of this model originally comes from the segregation behaviors of the alloying elements in superalloys. The assumption is that the as-built microstructure could be separated into the dendritic and interdendritic parts, where the composition differs from each other. In the AM processed alloys, the interdendritic region is considered as the vulnerable point which is the primary cracking (in-process cracking: solidification cracking and liquation cracking) source. On this basis, this additive manufacturability model focuses on the comparison of deformation resistance (strength) and heat resistance differences (melting temperature) between interdendritic and dendritic regions. Thus, if the interdendritic of one alloy shows close or even higher deformation and heat resistant capacity than the dendrite, the cracking susceptibility of this alloy is supposed to be lower. The additive manufacturability diagram revealed good agreement between the predicted additive manufacturability of the different superalloys with their experimental results. Targeting the processibility of LPBF as the top objective, two new superalloys were developed in this study. The first one is a high γ' -volume superalloy, MAD542, and the second one is an intermediate γ' -volume superalloy, Alloy738+. Both superalloys can be fabricated into the crack-free condition by using the optimized LPBF printing parameters.

2. To understand the microstructural evolution of high-strength nickel-based superalloys during the post-AM-treatments. To tailor the high-temperature mechanical properties by post-processing design.

Post-processing treatments significantly control the microstructures of LPBF superalloys. Thermal treatments at sub-solvus temperatures barely induce grain boundary migrations and the strong texture introduced by the printing process is stably retained. At the temperature above γ' solvus, recrystallized grains were developed, and crystallographic anisotropy was highly reduced but not fully eliminated. The underlying mechanism is that the lack of a strong enough driving force between the adjacent grains, and dragging force generated from the Zener pinning effect heavily retard the grain boundary migration at the sub-solvus temperature. Although the dendrite arm spacing is much finer in the LPBF superalloys, a sufficient dwell time at the solution temperature is required to complete the chemistry homogeneity. At least 2h at the super-solvus temperature was suggested in this study.

However, the recrystallized structure embrittles the vertically built LPBF superalloys at high temperatures, where the intergranular cracking is the dominated fracture mode. The relatively narrower γ channel in the super-solvus treated sample restricts the dislocation mean free path, i.e., decreases the capacity of deformation coordinated by dislocation gliding. After recrystallization, a larger portion of the transverse grain boundary was developed. Consequently, the grain boundary damages are prone to interlink along the transverse direction against loading direction, i.e., the anti-fracture capacity is reduced.

3. To examine the creep and oxidation properties of LPBF high-strength nickel-based superalloys. To understand the influence of minor elements addition on the time-dependent high-temperature deformation behaviors.

The most relevant creep temperature is 850 °C for testing the LPBF superalloys in this study. The building direction is the primary factor that determines the creep properties. The vertically built specimen obtains the slower minimum creep rate, larger creep ductility, and longer creep rupture time than the identical horizontally built LPBF superalloy. However, even vertically built superalloys show an apparent inferior creep performance than the castings. Grain boundary sliding with the assistance of dislocation activity is the dominant process for the creep deformation at this temperature. To this extent, the grain boundary strengthening elements are supposed to be beneficial for prolonging the elongation at fracture. However, these grain boundary elements demonstrate a double-edged sword effect on additive manufacturability and high-temperature mechanical properties. The reduction of grain boundary elements concentration significantly improves the crack resistance during the LPBF process, but on the other hand, decreases the ductility during high-temperature time-dependent deformation. Additionally, the short-term creep properties can be directly compared from the constant displacement rate-controlled slow strain rate tensile testing to constant stress-controlled creep testing.

Validated from the oxidation tests, both the new superalloys MAD542 and Alloy738+ demonstrate a low oxide growth rate at 850 °C and 950 °C. However, at the even higher temperature at 1050 °C, no effectively projective oxide layer was established. In addition, severe weight loss during cyclic oxidation at this temperature was found. To improve the

anti-spallation ability, purifying the concentration of trace elements and/or adding the alloying elements which increase the oxide scales adhesion, although these elements are considered to decrease the cracking resistance of superalloys for the LPBF process.

8.2 Outlook

For the newly designed superalloys, the materials development approach is rational and novel, the suggested alloys are highly cracking resistant during printing and the microstructure is of great potentiality for high-temperature properties. However, the mechanical properties, especially the low creep ductility, are not satisfactory at this stage and need further improvements. More efforts are worth putting into the future work regarding post-processing treatment optimization with the focus on improving the anti-fracture nature.

Another generally underestimated issue is the post-processing of LPBF components with complex geometry. In this study, the materials are mainly printed in a cube or cylinder shape, which is undoubtedly far from the real geometry for the application case. The high strain age cracking nature of high- γ' -volume nickel-based superalloy has been limited focused and slowed down the implementation of these materials to be deployed in the turbines. Either alloy development focusing on retardation of precipitation formation, or processing development on reducing the residual stress or the combination of both could be considered.

Bibliography

- [1] Standard, ISO/ASTM 52900 (2015).
- [2] I. Gibson, D.W. Rosen, B. Stucker, Additive Manufacturing Technologies, Springer US, Boston, MA, 2010.
- [3] SLM Solutions, <https://www.slm-solutions.com>.
- [4] EOS, <https://www.eos.info/en/additive-manufacturing/3d-printing-metal>.
- [5] GENERAL ELECTRIC, <https://www.ge.com/additive/who-we-are/concept-laser>.
- [6] TRUMPF, www.trumpf.com/en_INT/solutions/applications/additive-manufacturing/laser-metal-fusion.
- [7] GENERAL ELECTRIC, <https://www.ge.com/additive/direct-metal-laser-melting>.
- [8] GENERAL ELECTRIC, <https://www.ge.com/additive/ebm>.
- [9] S. Catchpole-Smith, N. Aboulkhair, L. Parry, C. Tuck, I.A.A. Ashcroft, A. Clare, Addit. Manuf. 15 (2017) 113–122.
- [10] C. Pauzon, E. Hryha, P. Forêt, L. Nyborg, Mater. Des. 179 (2019) 107873.
- [11] C. Pauzon, A. Leicht, U. Klement, P. Forêt, E. Hryha, Metall. Mater. Trans. A 51 (2020) 5339–5350.
- [12] D.D.T. Nayan Vinodbhai Patel, Fuel Nozzle For A Gas Turbine Engine, US 10,591,164 B2, 2020.
- [13] Joint Press Release by Siemens and ASME, <https://press.siemens.com/global/en/pressrelease/first-3d-printed-gas-turbine-blades-siemens-awarded-american-society-mechanical>.
- [14] R.F. Davis, in: Concise Encycl. Adv. Ceram. Mater., Elsevier, 1991, pp. 210–215.
- [15] M.T.T. Kim, S.Y.Y. Chang, J.B.B. Won, Mater. Sci. Eng. A 441 (2006) 126–134.
- [16] B. Rutttert, D. Bürger, L.M. Roncery, A.B. Parsa, P. Wollgramm, G. Eggeler, W. Theisen, Mater. Des. 134 (2017) 418–425.
- [17] H. Peng, Y. Shi, S. Gong, H. Guo, B. Chen, Mater. Des. 159 (2018) 155–169.
- [18] J. Xu, H. Gruber, R. Boyd, S. Jiang, R.L. Peng, J.J. Moverare, Materialia 10 (2020) 100657.
- [19] L.N. Carter, C. Martin, P.J. Withers, M.M. Attallah, J. Alloys Compd. 615 (2014) 338–347.
- [20] G.E. Fuchs, Mater. Sci. Eng. A 300 (2001) 52–60.
- [21] B.C. Wilson, J.A. Hickman, G.E. Fuchs, J. Miner. Met. Mater. Soc. 55 (2003) 35–40.
- [22] M. Ramsperger, L. Mújica Roncery, I. Lopez-Galilea, R.F. Singer, W. Theisen, C. Körner, Adv. Eng. Mater. 17 (2015) 1486–1493.
- [23] C. Körner, M. Ramsperger, C. Meid, D. Bürger, P. Wollgramm, M. Bartsch, G. Eggeler, Metall. Mater. Trans. A 49 (2018) 3781–3792.
- [24] O. Adegoke, J. Andersson, H. Brodin, R. Pederson, Metals (Basel). 10 (2020) 996.
- [25] K. Carpenter, A. Tabei, Materials (Basel). 13 (2020) 255.
- [26] J.P. Costes, Y. Guillet, G. Poulachon, M. Dessoly, Int. J. Mach. Tools Manuf. 47 (2007) 1081–1087.
- [27] P. Mercelis, J.P. Kruth, Rapid Prototyp. J. 12 (2006) 254–265.
- [28] J.A. Slotwinski, E.J. Garboczi, K.M. Hebenstreit, J. Res. Natl. Inst. Stand. Tech. 119 (2014) 494.
- [29] C. Weingarten, D. Buchbinder, N. Pirch, W. Meiners, K. Wissenbach, R. Poprawe, J. Mater. Process. Technol. 221 (2015) 112–120.
- [30] R. Xiao, X. Zhang, J. Manuf. Process. 16 (2014) 166–175.
- [31] E. Louvis, P. Fox, C.J. Sutcliffe, J. Mater. Process. Technol. 211 (2011) 275–284.
- [32] L. Rickenbacher, T. Etter, S. Hövel, K. Wegener, Rapid Prototyp. J. 19 (2013) 282–290.
- [33] D.G. Eskin, L. Katgerman, Metall. Mater. Trans. A 38 (2007) 1511–1519.

- [34] J. Zhang, R.F. Singer, *Acta Mater.* 50 (2002) 1869–1879.
- [35] C.E. Cross, in: *Hot Crack. Phenom. Welds*, Springer-Verlag, Berlin/Heidelberg, n.d., pp. 3–18.
- [36] B. Rogberg, *Scand. J. Metall.* 12 (1983) 51–66.
- [37] J.A. Spittle, A.A. Cushway, *Met. Technol.* 10 (1983) 6–13.
- [38] I. Farup, J.M. Drezet, M. Rappaz, *Acta Mater.* 49 (2001) 1261–1269.
- [39] W.S. Pellini, *Foundry* 80 (1952) 125–199.
- [40] J.P. Pumphrey WI, *J. Inst. Met.* 75 (1948) 235–256.
- [41] T. Böllighaus, H. Herold, C. Cross, J.C. Lippold, *Hot Cracking Phenomena in Wels II*, 2008.
- [42] M.C. Flemings, *Solidification Processing*, Mcgraw-Hill College, New York, 1974.
- [43] V. Shankar, T.P.S. Gill, S.L. Mannan, S. Sundaresan, *Sci. Technol. Weld. Join.* 5 (2000) 91–97.
- [44] G.M. Goodwin, *Weld. J.* 67 (1988) 88–94.
- [45] T. OGURA, S. ICHIKAWA, K. SAIDA, Q. J. JAPAN *Weld. Soc.* 34 (2016) 197–203.
- [46] E. Folkhard, *Welding Metallurgy of Stainless Steels*, Springer Vienna, Vienna, 1988.
- [47] V. Shankar, T.P.S. Gill, S.L. Mannan, S. Sundaresan, *Sadhana* 28 (2003) 359–382.
- [48] J. Grodzki, N. Hartmann, R. Rettig, E. Affeldt, R.F. Singer, *Metall. Mater. Trans. A* 47 (2016) 2914–2926.
- [49] M. Rappaz, A. Jacot, W.J. Boettinger, *Metall. Mater. Trans. A Phys. Metall. Mater. Sci.* (2003).
- [50] N. Wang, S. Mokadem, M. Rappaz, W. Kurz, *Acta Mater.* 52 (2004) 3173–3182.
- [51] J.C. Borland, *Br. Weld. J.* (1960) 508–512.
- [52] S. Edition, *Welding Metallurgy*, 2003.
- [53] S.L. West, W.A. Baeslack, T.J. Kelly, *Metallography* 23 (1989) 219–229.
- [54] M. Montazeri, F.M. Ghaini, *Mater. Charact.* 67 (2012) 65–73.
- [55] W.A. Baeslack, D.E. Nelson, *Metallography* 19 (1986) 371–379.
- [56] J.J. Pepe, W.F. Savage, *Weld. J.* (1967) 411–422.
- [57] J.J. Pepe, W.F. Savage, *Weld. J.* (1970) 545–553.
- [58] and C.P.S. W. A. Owczarski, D. S. Duvall, *Weld. J.* 45 (1966) 145–155.
- [59] D.S.D. and W.A. Owczarski, *Weld. J.* 46 (1967) 423–432.
- [60] S.G. R. G. Thompson, *Weld. J.* 62 (1983) 337–345.
- [61] D. Tomus, T. Jarvis, X. Wu, J. Mei, P. Rometsch, E. Herny, J.F. Rideau, S. Vaillant, in: *Phys. Procedia*, 2013, pp. 823–827.
- [62] A. Lingenfelter, *Superalloys 718 Metall. Appl.* (1989) 673–683.
- [63] O.A. Ojo, N.L. Richards, M.C. Chaturvedi, *Scr. Mater.* 50 (2004) 641–646.
- [64] H.A. Shahsavari, A.H. Kokabi, S. Nategh, *Mater. Sci. Technol.* 23 (2007) 547–555.
- [65] L. Thijs, K. Kempen, J.P. Kruth, J. Van Humbeeck, *Acta Mater.* 61 (2013) 1809–1819.
- [66] S.H. Sun, T. Ishimoto, K. Hagihara, Y. Tsutsumi, T. Hanawa, T. Nakano, *Scr. Mater.* 159 (2019) 89–93.
- [67] Z. Sun, X. Tan, S.B. Tor, C.K. Chua, *NPG Asia Mater.* 10 (2018) 127–136.
- [68] C.-H. Yu, R.L. Peng, V. Luzin, M. Sprengel, M. Calmunger, J.-E. Lundgren, H. Brodin, A. Kromm, J. Moverare, *Addit. Manuf.* (2020) 101672.
- [69] A. Basak, S. Das, *J. Alloys Compd.* 705 (2017) 806–816.
- [70] K. Kunze, T. Etter, J. Grässlin, V. Shklover, *Mater. Sci. Eng. A* 620 (2014) 213–222.
- [71] J. Xu, H. Gruber, D. Deng, R.L. Peng, J. Moverare, *Acta Mater.* 179 (2019) 142–157.
- [72] F. Geiger, K. Kunze, T. Etter, *Mater. Sci. Eng. A* 661 (2016) 240–246.
- [73] O.M.D.M. Messé, R. Muñoz-Moreno, T. Illston, S. Baker, H.J. Stone, *Addit. Manuf.* 22 (2018) 394–404.
- [74] M. Dahlén, L. Winberg, *Acta Metall.* 28 (1980) 41–50.
- [75] R. Muñoz-Moreno, V.D. Divya, S.L. Driver, O.M.D.M. Messé, T. Illston, S. Baker, M.A. Carpenter, H.J. Stone, *Mater. Sci. Eng. A* 674 (2016) 529–539.

- [76] J.N. Ghoussoub, P. Klupś, W.J.B. Dick-Cleland, K.E. Rankin, S. Utada, P.A.J. Bagot, D.G. McCartney, Y.T. Tang, R.C. Reed, *Addit. Manuf.* 52 (2022) 102608.
- [77] L.N. Carter, M.M. Attallah, R.C. Reed, in: *Superalloys 2012*, John Wiley & Sons, Inc., Hoboken, NJ, USA, 2012, pp. 577–586.
- [78] I.S. Kim, B.G. Choi, H.U. Hong, Y.S. Yoo, C.Y. Jo, *Mater. Sci. Eng. A* 528 (2011) 7149–7155.
- [79] A.J.J.M. G. A. YOUNG, T. E. CAPOBIANCO, M. A. PENIK, B. W. MORRIS, *Weld. Res.* (2008).
- [80] D. Qian, J. Xue, A. Zhang, Y. Li, N. Tamura, Z. Song, K. Chen, *Sci. Rep.* 7 (2017) 2859.
- [81] F.F. Noecker, J.N. Dupont, *Weld. Res.* 88 (2009).
- [82] W. Betteridge, S.W.K. Shaw, *Mater. Sci. Technol.* 3 (1987) 682–694.
- [83] J.K. Tien, T. Caulfield, *Superalloys, Supercomposites, and Superceramics*, Academic Press, 1989.
- [84] A.L. Marsh, *ELECTRIC RESISTANCE ELEMENT*, 811859, 1905.
- [85] D.E. Newton, *Chemistry of New Materials*, Facts on File, 2007.
- [86] The Home of HASTELLOY® and HAYNES® Alloys, Our Milestones, <http://www.haynesintl.com/company-information/our-heritage/our-milestones>.
- [87] F. Starr, *Int. J. Hist. Eng. Technol.* 84 (2014) 1–29.
- [88] C.G.C. L.B. Pfeil, N.B. Allen, *I.S.I. Spec. Rep.* (1952) 37–45.
- [89] H.L. Eiselstein, *Age-Hardenable Nickel Alloy*, US3046108A, 1962.
- [90] A.T. and R.W. Floyd, *J. Inst. Met.* (1952).
- [91] A.W.B. W. Franklin, *J. Inst. Met.* 85 (1957) 473–479.
- [92] M.C. Hardy, B. Zirbel, G. Shen, R. Shankar, in: *Proc. Int. Symp. Superalloys, 2004*, pp. 83–90.
- [93] R.C. Reed, Z. Zhu, A. Sato, D.J. Crudden, *Mater. Sci. Eng. A* 667 (2016) 261–278.
- [94] J.N. Ghoussoub, Y.T. Tang, C. Panwisawas, A. Németh, R.C. Reed, in: *Superalloys 2020*, *Miner. Met. Mater. Ser.*, 2020, pp. 153–162.
- [95] L.L. Sejournet Jacques, *EXTRUSION OF METALS*, US2538917A, 1948.
- [96] S. KAWAI, *Tetsu-to-Hagane* 63 (1977) 1975–1995.
- [97] F.I. Versnyder, M.E. Shank, *Mater. Sci. Eng.* 6 (1970) 213–247.
- [98] G.H. Gessinger, in: *Powder Metall. Superalloys*, Elsevier, 1984, pp. 3–15.
- [99] J. Xu, Z. Huang, L. Jiang, *Mater. Sci. Eng. A* 690 (2017) 137–145.
- [100] Y. Murata, K. Suga, N. Yukawa, *J. Mater. Sci.* 21 (1986) 3653–3660.
- [101] W.C.H. Chester T. Sims, Norman S. Stoloff, *Superalloys II: High-Temperature Materials for Aerospace and Industrial Power*, Wiley, 1987.
- [102] R.T. Holt, W. Wallace, *Int. Met. Rev.* 21 (1976) 1–24.
- [103] R.C. Reed, *The Superalloys Fundamentals and Applications*, Cambridge University Press, Cambridge, 2006.
- [104] M.J. Donachie, S.J. Donachie, *SUPERALLOYS A Technical Guide*, 2002.
- [105] M. Durand-Charre, *The Microstructure of Superalloys*, CRC Press, 1997.
- [106] H.A. Roth, C.L. Davis, R.C. Thomson, *Metall. Mater. Trans. A* 28 (1997) 1329–1335.
- [107] H.P. Karnthaler, E.T. Mühlbacher, C. Rentenberger, *Acta Mater.* 44 (1996) 547–560.
- [108] R.C. Reed, C.M.F. Rae, *Physical Metallurgy of the Nickel-Based Superalloys*, Fifth Edit, Elsevier B.V., 2014.
- [109] E.I. Galindo-Nava, L.D. Connor, C.M.F. Rae, *Acta Mater.* 98 (2015) 377–390.
- [110] W. Deng, D. Zhang, H. Wu, Z. Huang, K. Zhou, L. Jiang, *Scr. Mater.* 183 (2020) 139–143.
- [111] M. McLean, *Acta Metall.* 33 (1985) 545–556.
- [112] R.W. Kozar, A. Suzuki, W.W. Milligan, J.J. Schirra, M.F. Savage, T.M. Pollock, *Metall. Mater. Trans. A* 40 (2009) 1588–1603.
- [113] E.O. Hall, *Proc. Phys. Soc. Sect. B* 64 (1951).
- [114] N.J. Petch, *J. Iron Steel Inst.* 174 (1953) 25–28.

- [115] R.D.D. Bert Verlinden, Julian Driver, Indradev Samajdar, in: *Thermo-Mechanical Process. Met. Mater.*, Elsevier, 2007, pp. 55–81.
- [116] G.I. Taylor, *Proc. R. Soc. A Math. Phys. Eng. Sci.* 145 (1934) 362–387.
- [117] M.F.A. Harold J. Frost, *Deformation-Mechanisms Maps: The Plasticity and Creep of Metals and Ceramics*, Pergamon Press, 1982.
- [118] F.R.N. Nabarro, *Phys. Soc. London* (1948) 75–90.
- [119] C. Herring, *J. Appl. Phys.* 21 (1950) 437–445.
- [120] R.L. Coble, *J. Appl. Phys.* 34 (1963) 1679–1682.
- [121] T.H. Courtney, *Mechanical Behavior of Materials*, McGraw Hill, Boston, 2000.
- [122] R.C. Reed, T. Tao, N. Warnken, *Acta Mater.* 57 (2009) 5898–5913.
- [123] J.M. F.R. Larson, *Trans. ASME* 74 (1952) 765–771.
- [124] K. Kimura, *Mater. High Temp.* 25 (2008) 121–129.
- [125] K. Harris, G.L. Erickson, R.E. Schwer, *Superalloys 1984* (1984) 221–230.
- [126] J.B. Wahl, K. Harris, *Can. Metall. Q.* 50 (2011) 207–214.
- [127] M.N. Menon, P.T. Kantzos, D.J. Greving, in: *Proc. ASME Turbo Expo 2016 Turbomach. Tech. Conf. Expo. GT2016*, 2016, pp. 1–5.
- [128] M. Kaufman, *Superalloys 1984* (1984) 43–52.
- [129] A.K. Koul, R. Castillo, K. Willett, *Mater. Sci. Eng.* 66 (1984) 213–226.
- [130] T.P. Gabb, J. Gayda, A. Garg, in: *AIP Conf. Proc.*, AIP, 2007, pp. 640–651.
- [131] J. Xu, H. Gruber, R. Lin Peng, J. Moverare, *Materials* (Basel). 13 (2020) 4930.
- [132] H. Gruber, E. Hryha, K. Lindgren, Y. Cao, M. Rashidi, L. Nyborg, *Appl. Surf. Sci.* 573 (2022) 151541.
- [133] O. Adegoke, S.R. Polisetti, J. Xu, J. Andersson, H. Brodin, R. Pederson, P. Harlin, *Mater. Charact.* 183 (2022) 111612.
- [134] J.J.G. Clarence George Bieber, Suffern, *CAST NICKEL-BASE ALLOY*, 1969.
- [135] O. Adegoke, J. Andersson, H. Brodin, R. Pederson, *Materials* (Basel). 13 (2020) 3770.
- [136] F. Bachmann, R. Hielscher, H. Schaeben, *Solid State Phenom.* 160 (2010) 63–68.
- [137] I. 204:2009(E), (2009).
- [138] C.S.S. M. Prager, *Weld. Res. Council. Bull.* (1968) 1–55.
- [139] Y.T. Tang, C. Panwisawas, J.N. Ghoussoub, Y. Gong, J. Clark, A. Németh, D.G. McCartney, R.C. Reed, *Acta Mater.* (2020).
- [140] J. Campbell, *Castings*, 2nd Editio, Butterworth-Heinemann, 2003.
- [141] N. DSOUZA, H. DONG, M. ARDAKANI, B. SHOLLOCK, *Scr. Mater.* 53 (2005) 729–733.
- [142] G.J. Clyne, T.W., Davies, *Br. Foundrym.* 68 (1975) 238–244.
- [143] M. Rappaz, J.-M. Drezet, M. Gremaud, *Metall. Mater. Trans. A* 30 (1999) 449–455.
- [144] S. Griffiths, H. Ghasemi Tabasi, T. Ivas, X. Maeder, A. De Luca, K. Zweiacker, R. Wróbel, J. Jhabvala, R.E. Logé, C. Leinenbach, *Addit. Manuf.* 36 (2020) 101443.
- [145] S. Kou, *Acta Mater.* 88 (2015) 366–374.
- [146] J. Liu, S. Kou, *Acta Mater.* 125 (2017) 513–523.
- [147] J. Liu, H.P. Duarte, S. Kou, *Acta Mater.* 122 (2017) 47–59.
- [148] J. Liu, S. Kou, *Acta Mater.* 100 (2015) 359–368.
- [149] J. Liu, S. Kou, *Acta Mater.* 110 (2016) 84–94.
- [150] R. Li, M. Wang, Z. Li, P. Cao, T. Yuan, H. Zhu, *Acta Mater.* 193 (2020) 83–98.
- [151] N.J. Harrison, *Selective Laser Melting of Nickel Superalloys: Solidification, Microstructure and Material Response*, 2016.
- [152] N.J. Harrison, I. Todd, K. Mumtaz, *Acta Mater.* 94 (2015) 59–68.
- [153] A. Hariharan, L. Lu, J. Risse, A. Kostka, B. Gault, E.A. Jägle, D. Raabe, *Phys. Rev. Mater.* 3 (2019) 123602.

- [154] J.N. DuPont, J.C. Lippold, S.D. Kiser, *Welding Metallurgy and Weldability of Nickel-Base Alloys*, John Wiley & Sons, Inc., Hoboken, NJ, USA, 2009.
- [155] Y.T. Tang, J.N. Ghossoub, C. Panwisawas, D.M. Collins, S. Amirkhanlou, J.W.G. Clark, A.A.N. Németh, D. Graham McCartney, R.C. Reed, in: *Miner. Met. Mater. Ser.*, 2020, pp. 1055–1065.
- [156] A. Deshpande, S. Deb Nath, S. Atre, K. Hsu, *Metals (Basel)*. 10 (2020) 629.
- [157] X. Wang, L.N. Carter, B. Pang, M.M. Attallah, M.H. Loretto, *Acta Mater.* 128 (2017) 87–95.
- [158] V.D. Divya, R. Muñoz-Moreno, O.M.D.M. Messé, J.S. Barnard, S. Baker, T. Illston, H.J. Stone, *Mater. Charact.* 114 (2016) 62–74.
- [159] C.-H. Yu, R.L. Peng, M. Calmunger, V. Luzin, H. Brodin, J. Moverare, in: 2020, pp. 1003–1013.
- [160] T. Vilaro, C. Colin, J.D. Bartout, L. Nazé, M. Sennour, *Mater. Sci. Eng. A* 534 (2012) 446–451.
- [161] K.A. Christofidou, H.T. Pang, W. Li, Y. Pardhi, C.N. Jones, N.G. Jones, H.J. Stone, in: 2020, pp. 1014–1023.
- [162] N. Perevoshchikova, J. Rigaud, Y. Sha, M. Heilmaier, B. Finnin, E. Labelle, X. Wu, *Rapid Prototyp. J.* 23 (2017) 881–892.
- [163] H. Wang, X. Zhang, G.B. Wang, J. Shen, G.Q. Zhang, Y.P. Li, M. Yan, *J. Alloys Compd.* 807 (2019) 151662.
- [164] M. Cloots, K. Kunze, P.J. Uggowitzer, K. Wegener, *Mater. Sci. Eng. A* 658 (2016) 68–76.
- [165] Z. Chen, S. Chen, Z. Wei, L. Zhang, P. Wei, B. Lu, S. Zhang, Y. Xiang, *Prog. Nat. Sci. Mater. Int.* 28 (2018) 496–504.
- [166] L.N. Carter, X. Wang, N. Read, R. Khan, M. Aristizabal, K. Essa, M.M. Attallah, *Mater. Sci. Technol.* 32 (2016) 1–5.
- [167] G. Marchese, S. Parizia, M. Rashidi, A. Saboori, D. Manfredi, D. Ugues, M. Lombardi, E. Hryha, S. Biamino, *Mater. Sci. Eng. A* 769 (2020) 138500.
- [168] G. Marchese, M. Lorusso, S. Parizia, E. Bassini, J.-W. Lee, F. Calignano, D. Manfredi, M. Ternner, H.-U. Hong, D. Ugues, M. Lombardi, S. Biamino, *Mater. Sci. Eng. A* 729 (2018) 64–75.
- [169] D. Zhang, W. Niu, X. Cao, Z. Liu, *Mater. Sci. Eng. A* 644 (2015) 32–40.
- [170] M. Sadowski, L. Ladani, W. Brindley, J. Romano, *Addit. Manuf.* 11 (2016) 60–70.
- [171] Y.L. Kuo, S. Horikawa, K. Kakehi, *Scr. Mater.* 129 (2017) 74–78.
- [172] M. Cloots, P.J. Uggowitzer, K. Wegener, *Mater. Des.* 89 (2016) 770–784.
- [173] R. Engeli, T. Etter, S. Hövel, K. Wegener, *J. Mater. Process. Technol.* 229 (2016) 484–491.
- [174] H.M. Roman ENGELI, Thomas Etter, *Gamma Prime Precipitation Strengthened Nickel-Base Superalloy for Use in Powder Based Additive Manufacturing Process*, US 2017/0021453 A1, 2016.
- [175] C. Qiu, H. Chen, Q. Liu, S. Yue, H. Wang, *Mater. Charact.* 148 (2019) 330–344.
- [176] G. Marchese, S. Parizia, A. Saboori, D. Manfredi, M. Lombardi, P. Fino, D. Ugues, S. Biamino, *Metals (Basel)*. 10 (2020) 882.
- [177] J.H. Boswell, D. Clark, W. Li, M.M. Attallah, *Mater. Des.* 174 (2019) 107793.
- [178] N. Kalentics, N. Sohrabi, H.G. Tabasi, S. Griffiths, J. Jhabvala, C. Leinenbach, A. Burn, R.E. Logé, *Addit. Manuf.* 30 (2019) 100881.
- [179] Y. Hagedorn, J. Risse, W. Meiners, N. Pirch, K. Wissenbach, R. Poprawe, in: *High Value Manuf. Adv. Res. Virtual Rapid Prototyp.*, CRC Press, 2013, pp. 291–295.
- [180] I. Lopez-Galilea, B. Rutttert, J. He, T. Hammerschmidt, R. Drautz, B. Gault, W. Theisen, *Addit. Manuf.* 30 (2019) 100874.
- [181] K. Peng, R. Duan, Z. Liu, X. Lv, Q. Li, F. Zhao, B. Wei, B. Nong, S. Wei, *Materials (Basel)*. 13 (2020) 2149.
- [182] B. Wei, Z. Liu, B. Nong, B. Cao, X. Lv, Y. Ren, Y. Ai, *J. Alloys Compd.* 867 (2021) 158377.
- [183] A. Després, S. Antonov, C. Mayer, C. Tassin, M. Veron, J.-J. Blandin, P. Kontis, G. Martin, *Materialia* 19 (2021) 101193.

- [184] B. Wei, Z. Liu, B. Cao, B. Nong, Y. Zhang, Y. Ren, H. Zhou, S. Wei, J. Alloys Compd. (2021) 160413.
- [185] J. Yang, F. Li, A. Pan, H. Yang, C. Zhao, W. Huang, Z. Wang, X. Zeng, X. Zhang, J. Alloys Compd. 808 (2019) 151740.
- [186] S. Pourbabak, M.L. Montero-Sistiaga, D. Schryvers, J. Van Humbeeck, K. Vanmeensel, Mater. Charact. 153 (2019) 366–371.
- [187] O. Sanchez-Mata, X. Wang, J. Muñiz-Lerma, M. Attarian Shandiz, R. Gauvin, M. Brochu, Materials (Basel). 11 (2018) 1288.
- [188] N. Zhou, A.D. Dicus, S.A.J. Forsik, T. Wang, G.A. Colombo, M.E. Epler, in: TMS Superalloys 2020, 2020, pp. 1046–1054.
- [189] J. Xu, Alloy Design and Characterization of γ' Strengthened Nickel-Based Superalloys for Additive Manufacturing, Linköping University Electronic Press, 2021.
- [190] A. De Luca, C. Kenel, S. Griffiths, S.S. Joglekar, C. Leinenbach, D.C. Dunand, Mater. Des. 201 (2021).
- [191] S.P. Murray, K.M. Pusch, A.T. Polonsky, C.J. Torbet, G.G.E.E. Seward, N. Zhou, S.A.J.J. Forsik, P. Nandwana, M.M. Kirka, R.R. Dehoff, W.E. Slye, T.M. Pollock, Nat. Commun. 11 (2020) 4975.
- [192] J. Xu, F. Schulz, R.L. Peng, E. Hryha, J. Moverare, Results Mater. 12 (2021) 100232.
- [193] J.W. Cahn, Acta Metall. 10 (1962) 789–798.
- [194] M. Hillert, Acta Mater. 47 (1999) 4481–4505.
- [195] M. Hillert, B. Sundman, Acta Metall. 24 (1976) 731–743.
- [196] X. Wang, Z. Huang, B. Cai, N. Zhou, O. Magdysyuk, Y. Gao, S. Srivatsa, L. Tan, L. Jiang, Acta Mater. 168 (2019) 287–298.
- [197] N. Bozzolo, N. Souai, R.E. Logé, Acta Mater. 60 (2012) 5056–5066.
- [198] G.S.H. and H.K.D.H. Bhadeshia, in: Proc. Sheff. Centen. Conf. Perspect. Metall. Dev. Met. Soc., London, 1984, pp. 183–187.
- [199] X. Su, Q. Xu, R. Wang, Z. Xu, S. Liu, B. Liu, Mater. Des. 141 (2018) 296–322.
- [200] J. Xu, T. Ma, R.L. Peng, S. Hosseini, Addit. Manuf. 48 (2021) 102416.
- [201] M. Henthorne, CORROSION 72 (2016) 1488–1518.
- [202] ASTM G129, 2000.
- [203] Y.V.R.K. Prasad, H.L. Gegel, S.M. Doraivelu, J.C. Malas, J.T. Morgan, K.A. Lark, D.R. Barker, Metall. Trans. A 15 (1984) 1883–1892.
- [204] N. Srinivasan, Y.V.R.K. Prasad, Metall. Mater. Trans. A 25 (1994) 2275–2284.
- [205] H.T. Jeong, S.H. Han, W.J. Kim, J. Alloys Compd. 788 (2019) 1282–1299.
- [206] H.T. Jeong, H.K. Park, K. Park, T.W. Na, W.J. Kim, Mater. Sci. Eng. A 756 (2019) 528–537.
- [207] G.E. Dieter, Mechanical Metallurgy, McGraw-Hill, New York, 1988.
- [208] T.G. Langdon, Philos. Mag. 22 (1970) 689–700.
- [209] Z. Zhu, H. Basoalto, N. Warnken, R.C. Reed, Acta Mater. 60 (2012) 4888–4900.
- [210] D.J. Young, High Temperature Oxidation and Corrosion of Metals, Elsevier, Amsterdam, 2016.
- [211] W.J. Nowak, D. Naumenko, A. Jałowicka, D.J. Young, V. Nischwitz, W.J. Quadackers, Mater. Corros. 68 (2017) 171–185.
- [212] K.-S. Kim, S. Yang, M.-S. Kim, K.-A. Lee, J. Mater. Sci. Technol. 76 (2021) 95–103.
- [213] B.G. Cade, W.F. Caley, N.L. Richards, Can. Metall. Q. 53 (2014) 460–468.
- [214] F. Palmert, Oxidation and Degradation of Nickel-Base Alloys at High Temperatures, KTH Royal Institute of Technology, 2009.
- [215] H.T. Mallikarjuna, W.F. Caley, N.L. Richards, J. Mater. Eng. Perform. 26 (2017) 4838–4846.
- [216] M.P. Taylor, H.E. Evans, S. Stekovic, M.C. Hardy, Mater. High Temp. 29 (2012) 145–150.
- [217] S. Cruchley, H.E. Evans, M.P. Taylor, M.C. Hardy, S. Stekovic, Corros. Sci. 75 (2013) 58–66.

Papers

The papers associated with this thesis have been removed for copyright reasons. For more details about these see:

<https://doi.org/10.3384/9789179292584>



FACULTY OF SCIENCE AND ENGINEERING

Linköping Studies in Science and Technology, Dissertations No. 2217, 2022
Department of Management and Engineering

Linköping University
SE-581 83 Linköping, Sweden

www.liu.se